Article

Loss of symmetric cell division of apical neural progenitors drives *DENND5A*-related developmental and epileptic encephalopathy

A list of authors and their affiliations appears at the end of the paper

Developmental and epileptic encephalopathies (DEEs) feature altered brain development, developmental delay and seizures, with seizures exacerbating developmental delay. Here we identify a cohort with biallelic variants in *DENND5A*, encoding a membrane trafficking protein, and develop animal models with phenotypes like the human syndrome. We demonstrate that DENND5A interacts with Pals1/MUPP1, components of the Crumbs apical polarity complex required for symmetrical division of neural progenitor cells. Human induced pluripotent stem cells lacking *DENND5A* fail to undergo symmetric cell division with an inherent propensity to differentiate into neurons. These phenotypes result from misalignment of the mitotic spindle in apical neural progenitors. Cells lacking DENND5A orient away from the proliferative apical domain surrounding the ventricles, biasing daughter cells towards a more fate-committed state, ultimately shortening the period of neurogenesis. This study provides a mechanism for *DENND5A*-related DEE that may be generalizable to other developmental conditions and provides variant-specific clinical information for physicians and families.

Developmental and epileptic encephalopathies (DEEs) are characterized by developmental delay and drug-resistant seizures. Abnormal neurodevelopmental outcomes are the result of both the underlying etiology and the negative impact of frequent epileptic activity on the developing brain[1]. Homozygous variants in *DENND5A* (DENN Domain Containing protein 5A), a gene encoding a protein expressed at high levels in the developing brain, have been linked to epileptic encephalopathy[2,3], but the function of the protein during development is unknown. The conserved protein modules found in DENND5A and previously identified protein-protein interactions suggest its involvement in membrane trafficking and signal transduction. DENND5A contains a DENN domain, an evolutionarily conserved protein module found in 18 human proteins that functions as a guanine nucleotide exchange factor (activator) for Rab GTPases[4], as well as two RUN (RPIP8 [RaP2 interacting protein 8], UNC-14 and NESCA [new molecule

containing SH3 at the carboxyl terminus]) domains that often interact with Rab family members[5]. Through the most N-terminal RUN domain (RUN1), DENND5A is an effector for the active form of Rab6[6–8], and through the more C-terminal RUN domain (RUN2), DENND5A interacts with sorting nexin 1 (SNX1), a protein involved in protein trafficking between endosomes and the trans-Golgi network[9,10]. A role for DENND5A in cell division and polarity has been suggested in HeLa cells[11] and a canine kidney model of cell polarity[12], and heterozygous *DENND5A* loss-of-function variants genetically predispose individuals to familial cutaneous melanoma due to SNX1-related protein trafficking deficits[13]. Whether and how cell division and polarity are affected during neurodevelopment with loss-of-function *DENND5A* variants has not been investigated.

The establishment and maintenance of apicobasal cell polarity is crucial in neural development. In early cortical development, polarized

✉ e-mail: peter.mcpherson@mcgill.ca

neuroepithelial cells (NECs) or apical radial glia (aRG) orient their apical plasma membranes toward a central fluid-filled lumen[14], with the apical membrane responding to cerebrospinal fluid dynamics in the developing lateral ventricles[15,16]. Perturbations in genes encoding proteins that make up tight junctions (TJ) and adherens junctions (AJ), which define the apical plasma membrane and are often involved in cell division mechanisms, are associated with developmental defects consistent with DEE[17–20]. For example, pathogenic recessive variants in the gene encoding the TJ protein occludin (*OCLN*) result in DEE due to defects in neural progenitor cell (NPC) symmetric cell division caused by impaired mitotic spindle formation and centrosome misalignment during mitosis[21,22]. Similarly, depletion of the TJ and AJ protein PALS1 (Protein Associated with Lin7 1) results in loss of symmetric cell division and enhanced cell cycle exit in NPCs[23] and retinal neuroepithelia[24], and de novo variants in PALS1 have also been linked to developmental delay and neurological abnormalities[19,23].

Proteins comprising the apical membrane-defining Crumbs (Crb) complex in NECs include CRB2, MUPP1 (Multi-PDZ Protein 1, also known as MPDZ) or PATJ (Pals1-Associated Tight Junction Protein), and PALS1, and have been extensively studied for their roles in cell polarization and tissue development[25,26]. Most research on the Crb complex focuses on the version of the complex containing PATJ rather than MUPP1, and the only study directly comparing the function of these two highly similar proteins concludes that PATJ is essential but MUPP1 is dispensable for establishing and maintaining TJs[27]. Ex vivo studies, however, reveal significant deficits in ependymal[28,29] and choroid plexus epithelial cells[30] upon loss of MUPP1, including a complete loss of PALS1 expression in ependymal cells of *MUPP1* KO mice[29]. Although ependymal cells do not have TJs[31] or stem cell properties[32], they derive from TJ-containing NECs that gradually transition into RG cells that rely on abundant AJ protein expression to maintain their progenitor identity and ability to divide symmetrically[21,23,33,34]. Indeed, MUPP1 may differ from PATJ in that it preferentially stabilizes AJs over TJs[27], which may suggest a RG-specific function for this complex during neural development.

Here we describe a cohort of 24 individuals from 22 families with biallelic *DENND5A* variants and determine their clinical presentations through a phenotypic survey answered by their treating clinicians. The surveys were coupled with MRI analysis when available. We also demonstrate that DENND5A interacts with both PALS1 and MUPP1. To gain insight into the function of DENND5A, we employ mouse and zebrafish models of *DENND5A*-related DEE and perform in vitro assays using *DENND5A* knockout (KO) hiPSCs. We reveal an inherent propensity for neural stem cells lacking *DENND5A* to differentiate into neurons. Combined with disruption of symmetric cell division due to misalignment of the mitotic spindle, loss of *DENND5A* pushes daughter cells toward a more fate-committed state and likely shortens the period of neurogenesis.

Results

Phenotypic characterization of individuals with biallelic *DENND5A* variants

Following our initial analysis of two families with DEE and variants in *DENND5A*, we identified a cohort of 24 people (11F, 13M, mean age = 9.0 years, *SD* = 6.0) from 22 families with biallelic *DENND5A* variants. Thirty unique *DENND5A* variants were identified across the 14 homozygous and 10 compound heterozygous individuals. Seven members of the cohort have at least one additional variant flagged as potentially causative. Tables 1 and 2 summarize each person in the cohort, including their participant IDs, gene variant(s), predicted American College of Medical Genetics and Genomics variant interpretations, allele frequencies obtained from the gnomAD v2.1.1 dataset (https://gnomad.broadinstitute.org), seizure types and response to anti-seizure medications, occipitofrontal circumferences (OFCs), calculated scores corresponding to neurological and developmental phenotypes, and

developmental outcomes. Pedigrees for participants 10, 15, and 16 were published previously[2]. None of the *DENND5A* point mutations in the cohort were found in the homozygous state among 140,000 individuals on gnomAD, a database that removes individuals affected by severe pediatric disease, indicating that biallelic pathogenic variants are likely incompatible with normal development. Twenty-five of the variants are found in the coding sequence, two are copy number variants (exon 1–14 duplication [NC_000011.9:(9171749_9172227)_(9316934_9321244)dup] and exon one deletion [NC_000011.10:g.9262758_9268826del]), and three are intronic variants located in splice sites (splice donor variants c.2283+1G>T and c.949+1G>A, and polypyrimidine tract variant c.950-20_950-17delTTTT). The coding variants span the length of the protein including nine in the DENN domain, two in the RUN1 domain, six in the PLAT domain, four in the RUN2 domain, and four in predicted linker regions between the folded modules (Fig. 1a).

Complete phenotypic data for each member of the cohort is available in Source Data. The phenotypes observed in more than 50% of individuals with biallelic *DENND5A* variants were seizures (21/24), microcephaly (16/24), ventriculomegaly (15/24), hypertonia (14/24), cerebral hypoplasia (13/24), and hyperreflexia (13/24); Fig. 1b. It is important to note that participants 8 (p.K485E/p.R1159W), 19 (p.P955L/p.T136R), and 20 (exon 1-14 dup) did not present with seizures. Participant 8 had a normal brain MRI and an autism spectrum disorder diagnosis requiring low levels of support, participant 20 exhibited global developmental delay with a normal brain MRI, and participant 19 presented with moderate intellectual disability but did not undergo neuroimaging.

Seizures were reported in 20/23 individuals, with an average age of onset of 4.8 months (SD = 5.9). Seizures typically onset within the first year of life with one patient experiencing their first seizure at 2 years of age. A funnel chart showing the frequencies of commonly reported seizure types is presented in Fig. 1c. Focal to bilateral tonic-clonic is the most prominent seizure type, diagnosed in 9 individuals. Focal tonic seizures followed in 7 reported cases, 4 of whom were known to have impaired awareness. Among the 6 individuals presenting with epileptic spasms, 3 had a generalized onset, 2 had a focal onset, and 1 had an unknown onset. Generalized tonic-clonic seizures were reported in 5 individuals, as were focal clonic seizures. Three of the cases with focal clonic seizures had documented impaired awareness. Three individuals had focal myoclonic seizures, of which 2 cases had impaired awareness. In general, when the information was available, most focal seizures were accompanied by an impairment in awareness, with only one case retaining awareness. Seizures were generally drug-resistant, but control was achieved in 6 cases with variable antiepileptic treatment. Anti-seizure medications variably helped, did not affect, or worsened seizures, as reported for each case in Table 2.

All cases of microcephaly in the cohort were primary, with no cases of secondary microcephaly reported. Although microcephaly appears to be a major feature of *DENND5A*-related DEE, OFC percentiles ranged considerably (*M* = 18.5, Mdn = 2.9, SD = 30.2, Min = < 1, Max = 97). Figure 1d presents a histogram depicting the distribution of known OFCs. One case of macrocephaly (participant 1) was reported, possibly secondary to their benign external hydrocephalus. Another case (participant 20) was noted to be "borderline" microcephalic with an OFC percentile of 4. Among the seven individuals with normal OFCs, six underwent neuroimaging and 5 had clinically significant reductions in gray and/or white matter, indicating that neurodevelopment was compromised in most cases even when head circumference was within normal limits.

Failure to meet key developmental milestones was almost universal in the cohort, evidenced by the fact that all but one (participant 8; p.K485E/p.R1159W) presented with or had a history of global developmental delay. Among cohort members assessed

Table 1 | Table indicating demographics, variant details with American College of Medical Genetics and Genomics classifications predicted by Franklin/Varsome, allele frequencies, and variants found in other genes flagged as potentially causative of the clinical condition in each cohort member

| ID	Sex, Age range (years)	*DENND5A* variant(s)	Predicted ACMG classification	Allele frequency	Other gene variants
1	M, 6–10	p.R698W p.N1017S	*VUS* *VUS*	2.78×10^{-5} 1.59×10^{-5}	*CNOT3 (VUS)*
2	F, 6–10	c.1453A>G/p.K485E c.2129G>A/p.R710H	*LB/VUS* *LB/VUS*	7.08×10^{-4} 5.17×10^{-5}	-
3	M, 16–20	c.611_612insG/p.K205X	*LP*	N/A	-
4[3]	F, 6–10	c.1622A>G/p.D541G	*VUS*	N/A	-
5[3]	F, deceased 6–10	c.3811del/p.Q1271Rfs*67	*VUS/P*	N/A	-
7	F, 11–15	c.1363T>C/p.S455P c.3733G>A/p.A1245T	*VUS* *LB/VUS*	N/A 7.96×10^{-6}	*PEX1 (P)*
8	M, 11–15	c.1453A>G/p.K485E c.3475C>T/p.R1159W	*LB/VUS* *VUS*	7.08×10^{-4} 9.20×10^{-5}	*HERC2 (VUS), MYBPC3 (P)*
9	F, deceased 0–5	c.950-20_950-17delTTTT c.3233G>A/p.R1078Q	*LB* *LB/VUS*	4.06×10^{-5} 2.62×10^{-4}	*TBCK (LB/VUS)*
10[2]	F, 11–15	c.2547del/p.K850Sfs*11	*P*	N/A	-
12	M, 0–5	c.2314C>T/p.R772X c.3013T>A/p.L1005M	*P* *VUS*	3.19×10^{-5} N/A	CNV: 697 kb gain 6q25.3
14	M, 0–5	c.2180dupG/p.S728fs*34	*P*	N/A	-
15[2]	F, 11–15	c.517_518delGA/ p.D173Qfs*8	*P*	N/A	-
16[2]	F, deceased	c.517_518delGA/ p.D173Qfs*8	*P*	N/A	-
18	F, 16–20	c.2283+1G>T c.3018dupG/ p.K1007Efs*10	*VUS/LP* *LP*	N/A N/A	-
19	M, 6–10	c.407C>G/p.T136R c.2864C>T/p.P955L	*VUS* *VUS*	N/A 1.59×10^{-5}	*CACNA1C (LP/P)*
20	M, 0–5	Exon 1-14 dup	*VUS*	N/A	-
21	M, 16–20	c.1549C>T/p.R517W Exon 1 del	*VUS* *LP*	7.96×10^{-6} N/A	-
22	M, 11–15	c.955C>T/p.Q319X	*P*	N/A	*CDH4 (VUS)*
23	M, 11–15	c.949+1G>A	*LP*	N/A	-
25	F, 0–5	c.3605del/p.V1202Afs*52	*LP*	N/A	-
26	M, 0–5	c.623G>A/p.C208Y	*VUS*	N/A	-
27	M, 0-5	c.949+1G>A	*LP*	N/A	-
28	F, 0–5	c.949+1G>A	*LP*	N/A	-
30	M, 0–5	c.3095G>C/p.Arg1032Thr c.3116C>A/p.Thr1039Asn	*VUS* *VUS*	N/A N/A	-

Source data are provided as a Source Data file.

after age 5, 9 had severe intellectual disability (ID), profound ID was reported for 3 individuals, moderate ID was observed in 2 cases, and one participant (8) had no ID. Of the individuals, 15/24 (63%) were nonverbal, 7/24 (29%) were limited to single-word speech, and 2/24 (8%) could speak in sentences. Eye contact was observed in 11 of 24 individuals (46%). Eight of twenty-four individuals (33%) could walk independently and 11/24 (46%) were able to reach for and grasp objects. Motor skills were assessed via a scoring system across the group (Supplementary Methods), where a low score corresponds to no or minimal motor skills. Motor capabilities were more severely affected in those with microcephaly ($M_{\text{Micro}} = 3.2$, $M_{\text{No micro}} = 7.2$, $SD_{\text{Micro}} = 3.5$, $SD_{\text{No micro}} = 3.4$, two-tailed Mann-Whitney U, $Z = -2.55$, $p = 0.011$; Fig. 1e). Additionally, those with biallelic missense variants in *DENND5A* ($M = 7.4$, SD = 3.7) had significantly higher motor scores compared to those with a combination of missense, frameshift, nonsense, intronic, or copy number variants ($M = 2.9$, SD = 3.0, Kruskal-Wallis $H = 7.02$, $p = 0.03$; Fig. 1f).

Table 2 | Clinical summary table indicating details regarding seizures, microcephaly, and developmental phenotypes for each individual in the cohort

ID	Seizures (drug resistant)	Seizure type(s)	Medications that controlled, [did not affect], or (worsened) seizures	Microcephaly (OFC %ile)	Scores			Developmental outcome
					Communication	Motor	Neuro	
1	Y (N)	Unclassified (described as infantile spasms and focal left hemisphere involvement)	Vigabatrin, levetiracetam, [ACTH]	N (97)	2	10	2	Moderate ID
2	Y (Y)	Generalized epileptic spasms, generalized atonic	[prednisolone, vigabatrin, clobazam, lamotrigine, levetiracetam, felbamate, rufinamide, VNS therapy]	Y (<3)	4	0	4	Profound ID
3	Y (Y)	Generalized tonic-clonic	Valproic acid, lamotrigine, ativan, clobazam	Y (UK, −8.9 SD)	6	6	9	Profound ID
4[3]	Y (Y)	Focal impaired awareness tonic-clonic; focal to bilateral tonic-clonic	Levetiracetam, carbamazepine, clonazepam, topiramate, vigabatrin [(phenobarbital)]	Y (<3)	0	3	3	GDD (assessed age <5 y)
5[3]	Y (Y)	Focal aware tonic-clonic; focal to bilateral tonic-clonic	Phenobarbital, levetiracetam, [carbamazepine]	Y (<3)	1	0	10	GDD (assessed age <5 y)
7	Y (N)	Focal impaired awareness automatism, clonic, and atonic; generalized tonic-clonic	No medication	N (51)	4	9	4	Severe ID
8	N	N/A	N/A	N (90)	9	10	1	No GDD/ID
9	Y (Y)	Focal behavior arrest; unclassified (described as infantile spasms, myoclonic, and atonic seizures)	Topiramate, ACTH, [vigabatrin, diazepam, dexamethasone, pyridoxine, CBD oil, clobazam, sabril, prednisone, levocarnitine]	N (14)	3	1	4	Severe ID
10[2]	Y (UK)	Generalized tonic-clonic	UK	Y (<1)	7	9	5	Severe ID
12	Y (N)	UK; seizure associated with hypoglycemia	Phenobarbital, levetiracetam, CBD oil	Y (<1)	5	2	2	GDD
14	Y (Y)	Focal tonic and myoclonic; generalized absence	Levetiracetam, valproic acid	Y (<1)	1	0	10	GDD
15[2]	Y (Y)	Focal impaired awareness tonic and myoclonic; focal to bilateral tonic-clonic	Temporary (~3 mo) control with lamotrigine	N (50)	3	3	7	Severe ID
16[2]	Y (Y)	Focal impaired awareness tonic and myoclonic; focal to bilateral tonic-clonic	Temporary (~3 mo) control with lamotrigine	Y (<2)	3	2	7	Severe ID
18	Y (Y)	focal impaired awareness clonic and tonic; focal epileptic spasms; focal to bilateral tonic-clonic; focal impaired awareness behavior arrest; generalized motor onset myoclonic and tonic; unknown onset epileptic spasms; unknown onset behavior arrest	Vigabatrin, valproic acid, levetiracetam, [phenobarbital, sultiame]	Y (<1)	2	0	6	Profound ID
19	N	N/A	N/A	N (50)	9	9	No imaging	Moderate ID
20	N	N/A	N/A	N (4)	2	7	0	GDD
21	Y (Y)	Focal tonic; focal impaired awareness; focal to bilateral tonic-clonic	Current trial: clobazam, lamotrigine, CBD oil, [previous trials: levetiracetam, lacosamide, topiramate, sodium valproate, pyridoxine, gabapentin]	Y (<3)	6	8	4	Severe ID
22	Y (Y)	Focal impaired awareness clonic; focal to bilateral tonic-clonic	Sodium valproate, phenobarbital, [levetiracetam, (carbamazepine)]	Y (<3)	2	8	4	Severe ID
23	Y (Y)	Focal impaired awareness tonic; focal to bilateral tonic-clonic	Carbamazepine, sodium valproate, clobazam	Y (UK)	1	0	4	Severe ID
25	Y (Y)	Focal tonic; focal epileptic spasms	Vigabatrin, sodium valproate, [phenobarbital, vitamin B6, clobazam, ACTH, perimidone, levetiracetam], (phenytoin)	Y (<3)	1	0	9	GDD
26	Y (N)	Generalized epileptic spasms	Ommacortil, levetiracetam	Y (<3)	7	9	1	GDD
27	Y (N)	Generalized tonic-clonic	Levetiracetam, sodium valproate	Y (<3)	0	2	5	Severe ID
28	Y (N)	Focal impaired awareness clonic; focal to bilateral tonic-clonic; generalized tonic-clonic	Levetiracetam, sodium valproate	Y (<3)	0	3	5	GDD
30	Y (Y)	Generalized epileptic spasms	ACTH, sodium valproate, [vigabatrin, topiramate, phensuximide, nitrazepam], (lamotrigine)	N (UK)	7	9	5	GDD

Source data are provided as a Source Data file.
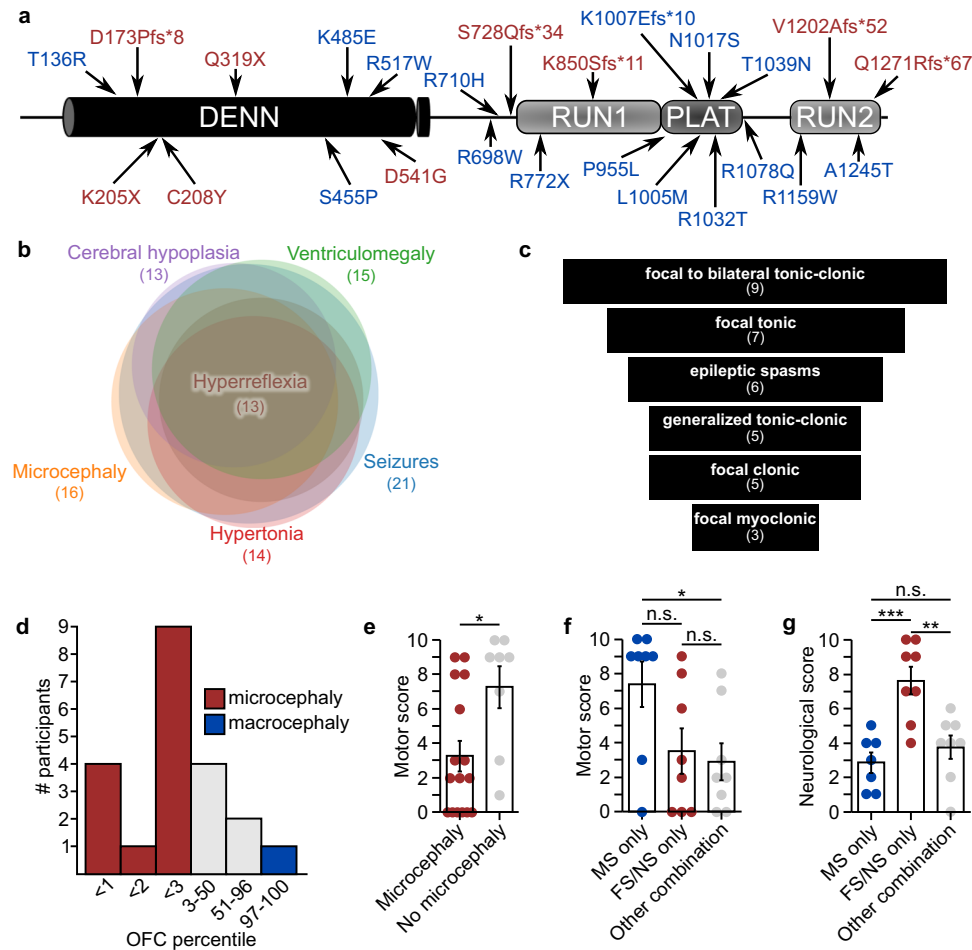
**Fig. 1 | *DENND5A* loss of function variants influence neurodevelopment.**
a Schematic of DENND5A protein with all coding sequence variants identified in the study. Red = found in homozygous individuals, blue = found in compound heterozygous individuals. **b** Venn chart showing the number of people with biallelic *DENND5A* variants exhibiting the most frequently reported phenotypes and the degree of phenotypic overlap between cohort members. **c** Funnel chart showing the most common seizure types present in the cohort. **d** Histogram depicting the number of individuals in a given OFC percentile range. Note that the exact OFC percentile is not known in every case. **e** Quantification of motor scores from $n = 16$ individuals with microcephaly and $n = 8$ individuals without microcephaly. Each dot represents one person. Data are mean ± SEM analyzed via two-tailed Mann-Whitney U test ($Z = -2.55$, $p = 0.011$). **f** Quantification of motor scores from $n = 8$ individuals

with biallelic missense variants, $n = 8$ individuals with biallelic frameshift or nonsense variants, and $n = 8$ individuals with an allelic combination of frameshift, nonsense, missense, intronic, or copy number variants in DENND5A. Each dot represents one person. Data are mean ± SEM analyzed via Kruskal-Wallis test followed by pairwise comparisons with Bonferroni corrections for multiple comparisons ($H(2) = 7.02$, $p = 0.03$). **g** Quantification of neurological scores from $n = 8$ individuals with biallelic missense variants, $n = 8$ individuals with biallelic frameshift or nonsense variants, and $n = 8$ individuals with an allelic combination of frameshift, nonsense, missense, intronic, or copy number variants in DENND5A. Each dot represents one person. Data are mean ± SEM analyzed via one-way ANOVA followed by Tukey's HSD ($F(2, 20) = [12.996]$, $p = 0.0002$). Source data for each panel are provided as a Source Data file.

MRIs or computed tomography (CT) scans revealed abnormalities in 20 of the 23 cases that underwent imaging. Normal MRIs were reported for participants 8, 20, and 26. We devised a scoring system (Supplementary Methods) to analyze the extent of neurological phenotypes across the group and found that variant type influences neurological phenotype severity, with more abnormalities in individuals with biallelic frameshift or nonsense variants ($M = 7.6$, SD = 2.3) compared to those with biallelic missense variants ($M = 2.8$, SD = 1.6, $p = 0.0004$) or another combination of variant types ($M = 3.8$, SD = 1.9, $p = 0.002$, one-way ANOVA, $F(2, 20) = [12.996]$, $p = 0.0002$; Fig. 1g). No significant difference in neurological score was observed between those with biallelic missense variants and those with a combination of missense, nonsense, frameshift, intronic, or copy number variants ($p = 0.657$).

Not all MR/CT images were made available, but all available images are presented in Fig. 2. Raw MRI data from five cases and raw CT data from one case were analyzed by a pediatric neuroradiologist. Of

these cases, two unrelated individuals (participants 5 and 14), both homozygous for *DENND5A* frameshift variants, showed the most extensive neuroanatomical phenotypes. These include severe dysgenesis of the basal ganglia with an indistinct and dysplastic thalamic transition, diencephalic-mesencephalic junction dysplasia, and cortical malformations, particularly with pachygyria involving the occipital lobes, a reduced volume of the white matter with associated striatal and periventricular calcifications and ventriculomegaly, agenesis or severe dysplasia/hypoplasia of the corpus callosum, thin anterior commissure, and variable degrees of pontocerebellar hypoplasia (Fig. 2a, b). The remaining cohort members with available images heterogeneously show subsets of these anatomical features. MRIs analyzed from two compound heterozygous cases that exhibited severe DEE (participants 2 and 18) showed relatively mild neuroanatomical phenotypes. Both exhibited mild volume loss, ventriculomegaly, dysgenesis or agenesis of the corpus callosum, and thin anterior commissure (Fig. 2c, d). Participant 2 showed diffuse gyral
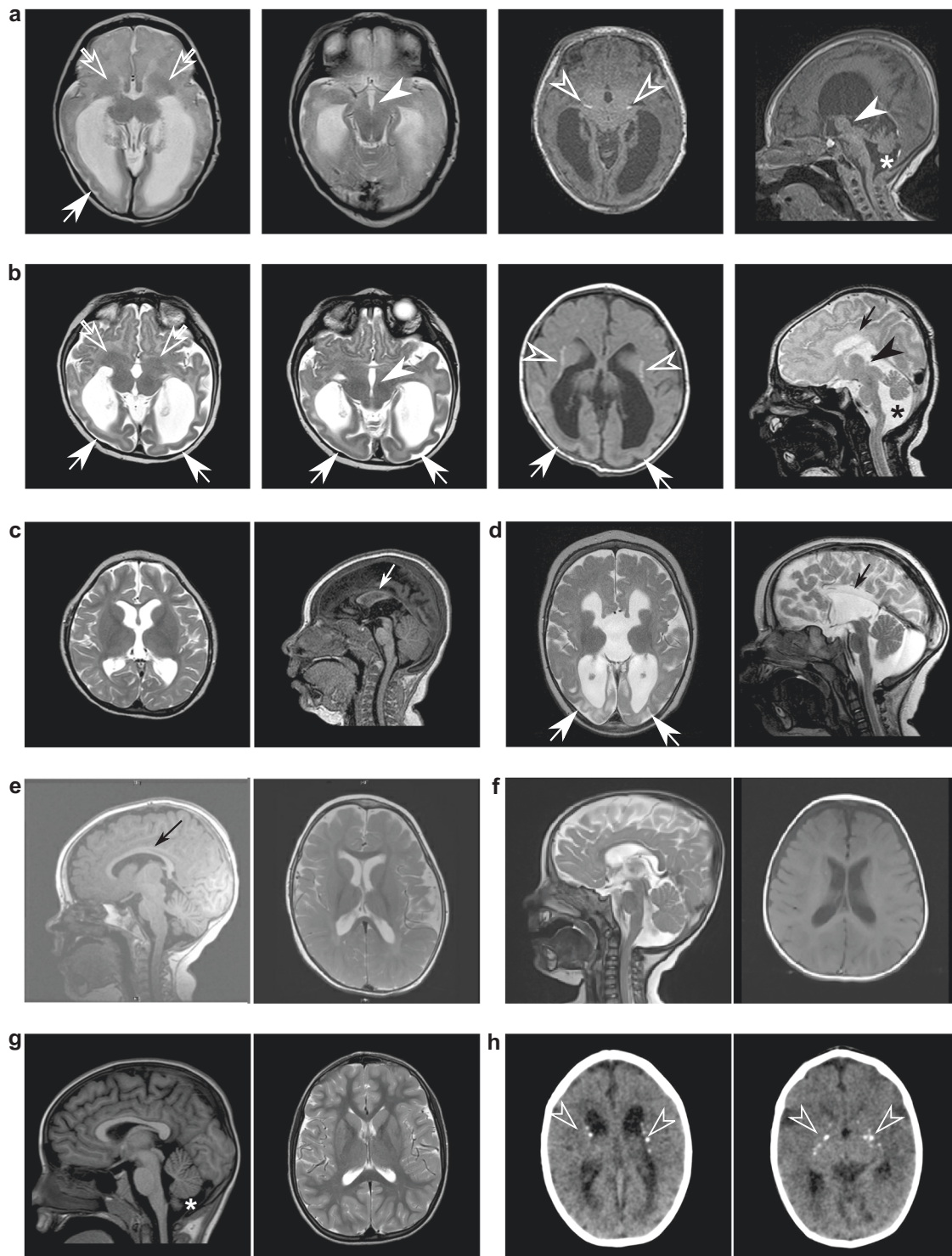
Fig. 2 | Neuroanatomical heterogeneity in individuals with biallelic *DENND5A* variants. Representative MRI slices from unrelated individuals with (**a**) homozygous p.Q1271R*67 variants (participant 5); (**b**) homozygous p.S728Qfs*34 variants (participant 14); (**c**) compound heterozygous p.K485E/p.R710H variants (participant 2); (**d**) compound heterozygous c.2283+1 G > T/p.K1007Efs*10 variants (participant 18); (**e**) compound heterozygous individual with variants c.950-20_950-17delTTTT/p.R1078Q (participant 9); (**f**) compound heterozygous individual with variants p.R1032T/p.T1039N (participant 30); and (**g**) compound heterozygous individual with variants p.K485E/p.R1159W (participant 8). **h** CT images from a homozygous individual with the variant p.V1202Afs*52 (participant 25). Arrows = posterior gradient of pachygyria/lissencephaly; open arrows = basal ganglia dysmorphism; arrowheads = diencephalic/mesencephalic junction dysplasia; open arrowheads = calcifications; small arrows = corpus callosum dysgenesis/agenesis; asterisks = cerebellar hypoplasia.

simplification (Fig. 2c), and participant 18 presented with basal ganglia dysmorphism and a posterior gradient of gyral simplification with occipital encephalomalacia (Fig. 2d). Raw MRI data from compound heterozygous participants 9 and 30 were not available, but isolated images revealed mild hypoplasia of the corpus callosum (Fig. 2e) and ventriculomegaly (Fig. 2f), respectively. Participant 8 with variants p.K485E/p.R1159W had a normal MRI with only mild inferior cerebellar vermis hypoplasia (Fig. 2g). Finally, CT image analysis of another

homozygous individual with severe DEE also revealed ventriculomegaly, a hypoplastic corpus callosum, mild cerebral hypoplasia, and lenticulostriate and periventricular calcifications (Fig. 2h). These imaging studies highlight the heterogenous neuroanatomical manifestations of biallelic *DENND5A* variants, but certain features including volume loss, ventriculomegaly, and hypoplasia of the corpus callosum appear more frequently.

DENND5A expression analysis

DENND5A protein levels were determined in cell lines derived from five cohort members: three from NPCs differentiated from induced pluripotent stem cells (hiPSCs), and two from immortalized lymphoblasts, with homozygous and compound heterozygous as well as frameshift, nonsense, and missense variants represented. Positive controls (i.e., cells derived from healthy donors) were used in both experiments, and hiPSC-derived cells were additionally compared against a negative control cell line in which KO of *DENND5A* was generated with CRISPR/Cas9 using guide RNAs targeting exon four. NPCs express SOX1, SOX2, and Nestin, affirming their NPC identity (Supplementary Fig. 1). All patient-derived cells exhibit a reduction in DENND5A protein (Supplementary Fig. 2a, b), supporting that disease phenotypes are a result of protein loss of function; however, the KO-validated DENND5A antibody recognizes a region of the protein more C-terminal to the stop codon of p.K205X. RT-qPCR was thus performed. A rather poor correlation between *DENND5A* mRNA and protein levels was observed as *DENND5A* mRNA expression from patient-derived cells did not differ significantly from controls (Supplementary Fig. 2c, d). This includes NPCs with homozygous p.K850Sfs*11 variants, where the antibody can determine that a ~100 kDa truncated protein is not expressed because its epitope should still be detected, but mRNA levels were comparable to WT NPCs. When introduced into a FLAG-tagged DENND5A plasmid construct and overexpressed in HEK293T cells, p.K205X resulted in no detectable protein, indicating that even if a truncated protein is produced it is rapidly degraded (Supplementary Fig. 2e). It is important to note, however, that the generalizing power of overexpression studies to evaluate variants of uncertain clinical significance (VUSs) is limited. mRNA derived from plasmid DNA does not undergo the same RNA processing that endogenous DENND5A would experience because it lacks introns, and therefore the evaluation of protein expression based on overexpression studies alone does not substantially contribute to the interpretation of VUSs other than revealing the overall biochemical stability of the translated protein.

Characterization of *DENND5A*-related DEE animal models

We established animal models in mice and zebrafish to study how biallelic pathogenic *DENND5A* variants affect development. A knock-in (KI) mouse model, homozygous for a frameshift variant (c.517_517delGA/p.D173Pfs*8) found in the proband of *DENND5A*-related DEE[2] (participants 15 and 16) and conserved in mice (Supplementary Fig. 3a, b), exhibits anatomical and functional phenotypes consistent with those found in our human cohort. Immunoblotting indicated that full-length DENND5A protein is not expressed in KI mice (Fig. 3a). Similarly to our patient-derived samples, RT-qPCR did not reveal a significant difference in *DENND5A* mRNA expression ($M_{WT}=1.0$, $M_{KI}=0.67$, $SD_{WT}=0.68$, $SD_{KI}=0.42$, two-tailed Mann-Whitney U, $Z=-1.81$, $p=0.077$; Fig. 3b). However, DENND5A protein containing the mutation and tagged at the N-terminus with FLAG is degraded when overexpressed in HEK-293T cells (Supplementary Fig. 2e), indicating that even if translated, the protein is likely degraded. In vivo 7T MRI scans revealed that *DENND5A* KI mice have significantly enlarged lateral ventricles ($M_{WT}=4.8$ mm³, $M_{KI}=6.6$ mm³, $SD_{WT}=1.3$, $SD_{KI}=2.4$, two-tailed Mann-Whitney U, $Z=-2.117$, $p=0.034$), consistent with ventriculomegaly (Fig. 3c, d). KI mice also have a lower mean and median relative brain sizes, but like the human cohort in which occipitofrontal circumference percentiles varied

considerably, a high degree of variability was observed in the mice and the difference did not reach statistical significance ($M_{WT}=1.03$, $Mdn_{WT}=1.04$, $M_{KI}=0.97$, $Mdn_{KI}=0.94$, $SD_{WT}=0.08$, $SD_{KI}=0.10$, two-tailed Mann-Whitney U, $Z=-1.361$, $p=0.174$; Fig. 3e). Finally, while spontaneous seizures were not observed in the KI mice, they show increased seizure susceptibility compared to WT when administered the potassium channel blocker 4-aminopyridine ($M_{WT}=23.60$, $M_{KI}=11.67$, $SD_{WT}=2.97$, $SD_{KI}=7.20$, two-tailed $t(9)=3.445$, $p=0.007$; Fig. 3f).

A zebrafish model system was developed to study DENND5A during development. *dennd5a* mRNA was detected throughout embryonic development beginning from the first-hour post-fertilization (hpf) (Supplementary Fig. 3c), and in situ hybridization revealed *dennd5a* expression at the two-cell stage (Fig. 3g). The mRNA was enriched in the central nervous system, retinal ganglion cells (RGCs), the sensory epithelium (otic vesicle, Ov), pharyngeal cephalic musculature (Cm), and the heart (H), as detected 24, 48, and 72 hpf (Fig. 3h–j). Biallelic mutations in *dennd5a* were introduced into zebrafish larvae using CRISPR/Cas9 (F_0 KOs). Successful KO was confirmed by measuring *dennd5a* mRNA via RT-qPCR compared to Cas9 protein-injected controls (Supplementary Fig. 3d). F_0 KOs show structural and behavioral perturbations consistent with *DENND5A*-related DEE including reduced head size and increased ventricle size (Fig. 3k–n). Moreover, the fish display behavioral phenotypes indicating neurological deficits, including altered locomotor activity during periods of light and dark and reductions in visual and acoustic startle responses (Supplementary Fig. 3e–h). Eye size is also reduced in F_0 KOs (Supplementary Fig. 3i). Taken together, loss of *DENND5A* leads to conserved developmental alterations in multiple animal models.

DENND5A interacts with protein components of apical polarity Crumbs complex

We screened for DENND5A binding partners using affinity purification with multiple regions and domains of the protein as bait. Mass spectrometry of purified proteins revealed members of the Crb polarity complex, MUPP1, and PALS1, as major DENND5A binding partners, with the interaction mediated via a GST-tagged peptide flanking the missense variant R710H (Fig. 4a, b). This interaction was confirmed with proteins expressed in HEK293T cells (Fig. 4c).

We modeled the predicted structure of DENND5A from AlphaFold[35,36] and noted that residues R701, E707, H708, R710, and R716, in the region of DENND5A interacting with the polarity proteins, have predicted intramolecular interactions with residues of the DENN domain, making hydrogen bonds with residues S10-A11, R273, R129, and D598 (Fig. 4d). This suggests a conformational change in DENND5A is necessary to expose the binding site for MUPP1/PALS1. In fact, full-length DENND5A has limited interaction with these proteins (Fig. 4g). Because DENN domains are evolutionarily conserved protein modules that function as guanine nucleotide exchange factors for Rab GTPases[4], we aligned the co-crystal structure of DENND1B and Rab35 with the predicted DENND5A structure and found that the predicted Rab enzymatic site in DENND5A may be occluded by interactions between the DENN and RUN1 (RPIP8, UNC-14 and NESCA)/PLAT (Polycystin-1, Lipoxygenase, Alpha-Toxin) domains (PDB: 3TW8[37]; Supplementary Fig. 4a). In contrast, a conformational change is not necessary for the known DENND5A binding partner GTP-Rab6 to bind the RUN1 domain (PDB: 3CWZ[7]; Supplementary Fig. 4b), suggesting that two functional conformations are both possible and necessary.

We next examined the intramolecular interactions blocking MUPP1/PALS1 binding in the AlphaFold structure of DENND5A and observed a cluster of highly charged residues at the interface of the DENN and RUN1 domains (Fig. 4e), suggesting that the structure can be biochemically manipulated to expose both the Rab and Crb complex
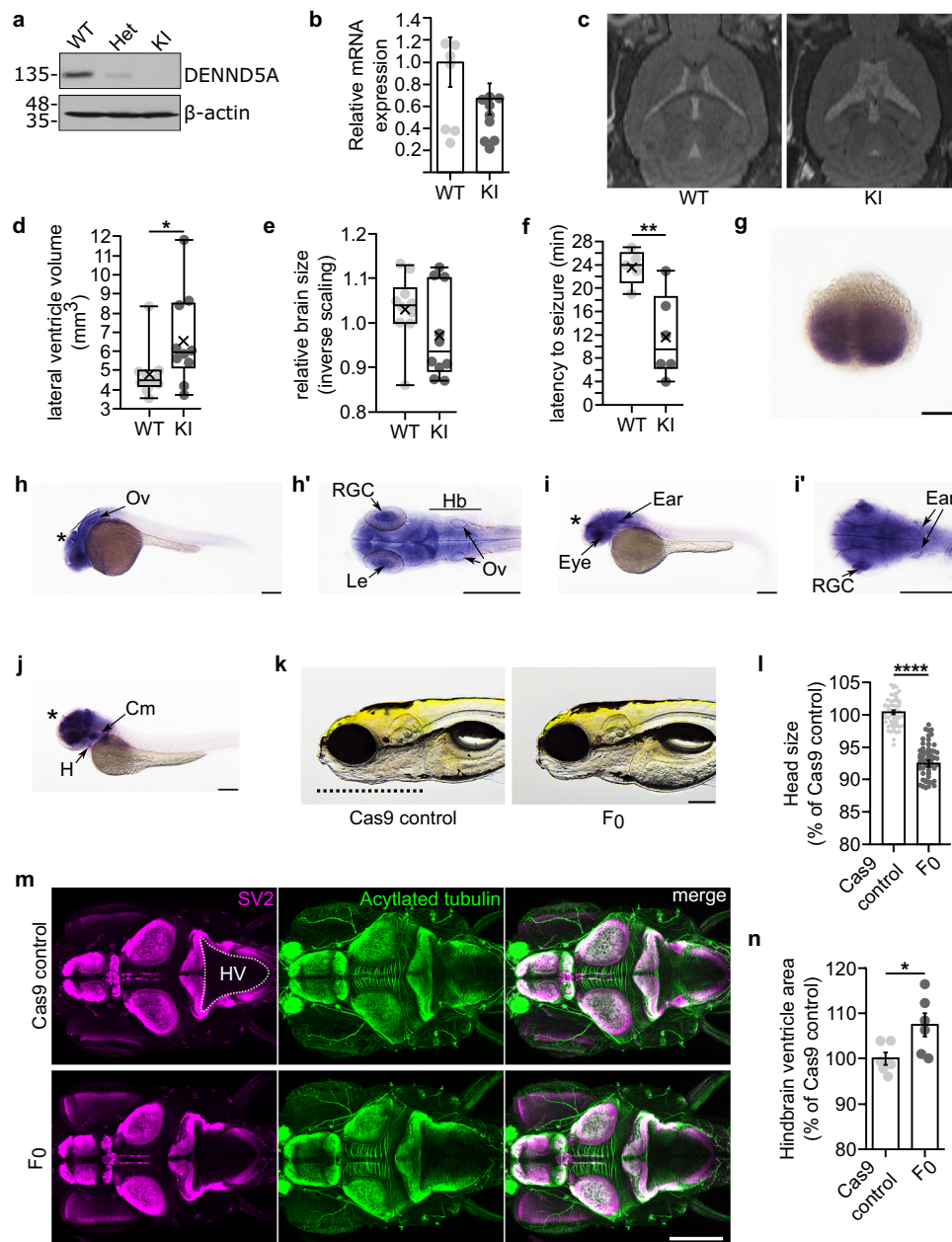
Fig. 3 | Animal models of *DENND5A*-DEE exhibit phenotypes consistent with the human cohort. a DENND5A protein levels in WT, heterozygous (Het), and homozygous knock-in (KI) mouse brains. Results were reproduced in three independent experiments. **b** *DENND5A* mRNA levels in $n = 6$ mouse brains. RT-qPCR was performed in triplicate in three independent experiments. Data are mean ± SEM (two-tailed Mann-Whitney U, $Z = -1.81$, $p = 0.077$). **c** Sample images of in vivo 7 T MRIs. **d** Quantification of pooled lateral ventricle volumes obtained through segmenting $n = 10$ MRIs (two-tailed Mann-Whitney U, $Z = -2.117$, $p = 0.034$). Each dot represents one animal. **e** Quantification of relative brain volumes using MRI data from $n = 10$ mice (two-tailed Mann-Whitney U, $Z = -1.361$, $p = 0.174$). Each dot represents one animal. **f** Quantification of seizure latency after 4-AP injection in $n = 5$ WT and $n = 6$ KI mice from three independent experiments (two-tailed student's $t(9) = 3.445$, $p = 0.007$). Each dot represents one animal. Whole-mount in situ hybridization

from two independent experiments shows *denndSa* mRNA expression at (**g**), 0.75 hpf, (**h**), 24 hpf, (**i**), 48 hpf and (**j**), 72 hpf. Asterisks brain, Ov otic vesicle, Le lens, RGC retinal ganglion cells, Hb hindbrain, H heart, Cm cephalic musculature. Scale bar = 0.2 mm. **k** Representative images of control and F_0 KO zebrafish from three independent experiments. Dotted line marks the length of the head used in quantification. Scale bar = 0.2 mm. **l** Quantification of head size in $n = 60$ larvae (two-tailed Mann-Whitney U, $Z = -9.206$, $p = 3.4 \times 10^{-20}$). Each dot represents one larva. **m** Representative image of larva at 6 dpf immunostained with anti-SV2 (magenta) and anti-acetylated tubulin (green). Dorsal view, anterior to the left. Dotted line outlines hindbrain ventricle (HV) area used in quantification. **n** Quantification of hindbrain ventricle area in $n = 6$ larvae (two-tailed student's $t(10) = -2.564$, $p = 0.028$). Each dot represents one larva. Source data for (**a**, **b**), (**d**, **f**), (**l**) and (**n**) are provided as a Source Data file.

binding sites. To confirm this intramolecular interaction experimentally, we performed a pull-down assay with the GST-RUN1/PLAT domains as bait in HEK293T lysate expressing either full-length FLAG-tagged DENND5A or the isolated DENN domain (aa1-680). Both DENND5A constructs bind the RUN1/PLAT domain, with a slightly stronger interaction with the isolated DENN domain (Fig. 4f).

Moreover, the DENN domain interaction was impeded with charge masking from higher salt concentrations (Supplementary Fig. 4c). We then performed mutagenesis experiments targeting residues involved in the intramolecular interaction. Mutating E379 of the DENN/RUN1 interface resulted in a weak but present interaction between full-length DENND5A and Crb complex proteins, implying that DENND5A
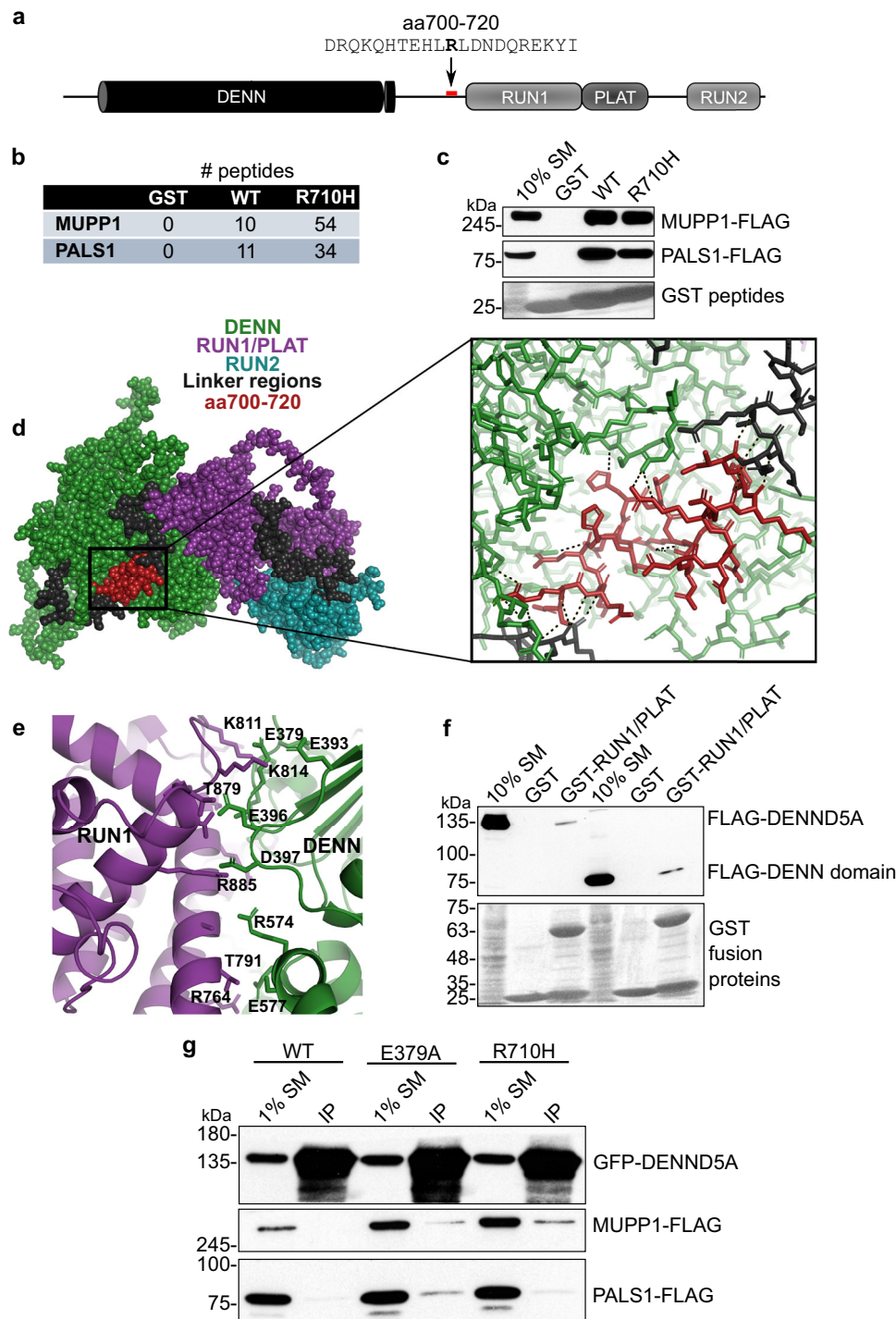
Fig. 4 | DENND5A interacts with polarity proteins MUPP1 and PALS1. a A recombinant GST-tagged peptide containing amino acids 700-720 of human DENND5A sequence was generated for use in pulldown experiments. The bolded residue corresponds to Arg710 that is affected in the cohort (R710H). **b** Table indicating the number of peptides corresponding to MUPP1 and PALS1 found bound to each GST fusion peptide used in the pulldown/mass spectrometry experiment. **c** Overexpressed human MUPP1- and PALS1-FLAG bind to GST-tagged DENND5A peptides. Results were reproduced in 3 independent experiments. **d** Residues 700–720 are shown in red in a space-fill model (left) and

magnified view (right) of the predicted DENND5A protein structure from Alpha-Fold. Dotted lines indicate hydrogen bonds. **e** The interface between the DENN and RUN1 domains of DENND5A comprises many charged residues. **f** GST pull-down experiments show that FLAG-DENN and GST-RUN1/PLAT physically interact. **g** Co-immunoprecipitations between GFP-DENND5A and MUPP1- and PALS1-FLAG show that DENND5A only binds the polarity proteins when the intramolecular DENN-RUN1 interaction is disrupted. Source data for (**b**, **c**) and (**f**, **g**) are provided as a Source Data file.

molecules with this mutation were skewed toward an open conformation (Fig. 4g). R710H, which lies in the region linking the DENN and RUN1 domains, is predicted to result in the loss of a salt bridge to D598 of the DENN domain, potentially destabilizing the closed

structure (Supplementary Fig. 4d). Like what was observed upon disrupting the DENN/RUN1 interaction, introducing the patient variant R710H resulted in increased binding to MUPP1-FLAG and PALS1-FLAG (Fig. 4g). We conclude that DENND5A binds MUPP1 and PALS1 in a

conformation-dependent manner, and that R710H increases the likelihood that DENND5A will adopt an open configuration.

Loss of DENND5A drives premature neuronal differentiation

Microcephaly in *PALS1* conditional KO mice is due to neural progenitors prematurely exiting the cell cycle and undergoing asymmetric neurogenic cell divisions instead of symmetric proliferative divisions, resulting in the depletion of the progenitor pool and premature neuronal differentiation[23]. Our discovery of an interaction between DENND5A and PALS1 implies a degree of shared function. We thus tested if DENND5A also regulates cell division and neuronal differentiation. We observed that *DENND5A* KO NPCs grow slower than WT (Fig. 5a). Interestingly, a significant difference was observed even after 24 h ($M_{WT} = 710$, $M_{KO} = 621$, $SD_{WT} = 108.8$, $SD_{KO} = 72.4$, two-tailed $t(18) = 2.168$, $p = 0.044$), likely due to an increased number of apoptotic cells observed in the KOs post-plating. WT NPCs then rapidly increased in number whereas the number of KO NPCs remained relatively stable, producing a significant difference after 48 ($M_{WT} = 1008$,
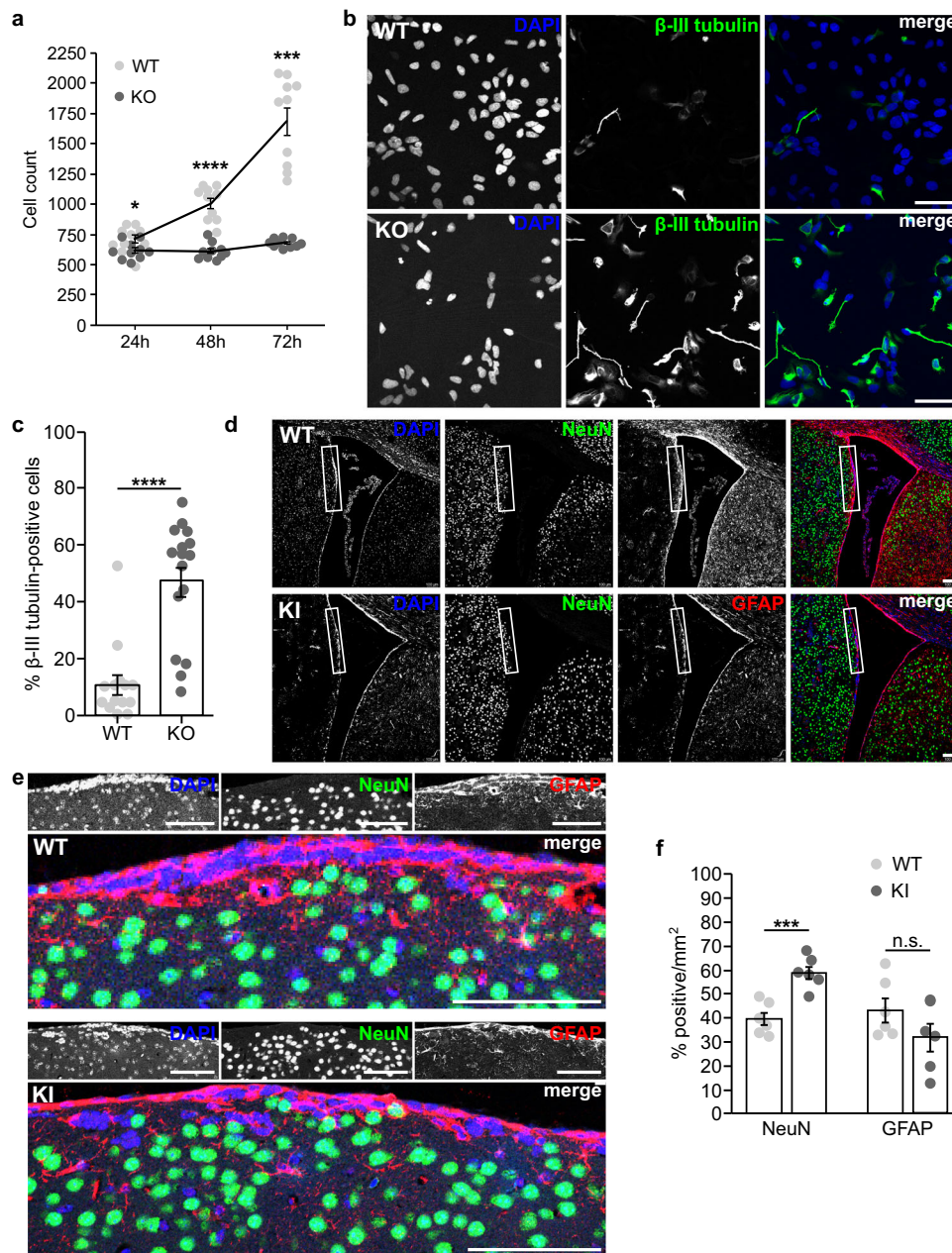
Fig. 5 | Loss of DENND5A results in premature neuronal differentiation. a Graph showing the average number of NPCs counted per well of a 96-well plate 24, 48, and 72 h after plating equal numbers of cells. Data are derived from 5 technical replicates from two independent experiments. Each dot represents the number of cells counted in one well. Data are mean ± SEM. 24 h: two-tailed $t(18) = 2.168$, $p = 0.044$; 48 h: two-tailed Welch's $t(12.96) = 8.30$, $p = 0.000002$; 72 h: two-tailed Mann-Whitney U, $Z = -3.78$, $p = 0.00016$. **b** Immunostaining of β-III tubulin (green) and DAPI (blue) in NPCs one day after plating into neural progenitor maintenance medium. Scale bar = 50 μm. **c** Quantification of the percent of β-III tubulin-positive cells per field. A total of $n = 2267$ cells were analyzed from three independent experiments. Each dot represents the percentage calculated from one image. Data are mean ± SEM analyzed via two-tailed Mann-Whitney *U*, $Z = -3.991$, $p = 0.000013$. **d** Immunostaining of GFAP (red), NeuN (green), and DAPI (blue) in the SVZ of adult mice. Scale bar = 100 μm. **e** Close-up of the regions indicated in the insets in (**d**). **f** Quantification of the percentage of cells per mm² labeled by NeuN or GFAP from a total of $n = 4$ mice. Each dot represents the percentage calculated from one image. Data are mean ± SEM. NeuN: two-tailed $t(10) = -4.981$, $p = 0.001$; GFAP: two-tailed $t(10) = 1.486$, $p = 0.168$. Source data for (**a**), (**c**), and (**f**) are provided as a Source Data file.

$M_{KO} = 614$, $SD_{WT} = 135.6$, $SD_{KO} = 65.30$, two-tailed Welch's $t(12.96) = 8.30$, $p < 0.0001$) and 72 h ($M_{WT} = 1685$, $M_{KO} = 683$, $SD_{WT} = 351.6$, $SD_{KO} = 35.09$, two-tailed Mann-Whitney U, $Z = -3.78$, $p < 0.0001$).

Remarkably, after passaging newly-formed NPCs into neural progenitor maintenance medium, KO NPCs develop β-III tubulin-positive processes with neuronal morphology after one day, something rarely observed in WT NPCs ($M_{WT} = 10.67\%$, $M_{KO} = 47.29\%$, $SD_{WT} = 13.5$, $SD_{KO} = 21.1$, two-tailed Mann-Whitney U, $Z = -3.991$, $p < 0.0001$; Fig. 5b, c). To determine if this premature differentiation phenotype translates to alterations in animals, we used our *DENND5A* KI mice to examine the adult subventricular zone (SVZ), a region that normally retains GFAP-positive RG-like neural stem cells[38], the primary source of newborn neurons in the adult brain[39]. KI mice have a significantly higher percentage of post-mitotic neurons expressing NeuN compared to WT mice ($M_{WT} = 39.6\%$, $M_{KI} = 58.8\%$, $SD_{WT} = 6.7$, $SD_{KI} = 6.6$, two-tailed $t(10) = -4.981$, $p = 0.001$; Fig. 5d–g). While there is also a reduction in the mean proportion of GFAP-positive cells in the SVZ of the KI mice, it did not reach significance ($M_{WT} = 43.3\%$, $M_{KI} = 31.9\%$, $SD_{WT} = 12.3$, $SD_{KI} = 14.1$, two-tailed $t(10) = 1.486$, $p = 0.168$). Our results suggest that DENND5A expression promotes stemness and its loss drives cell cycle exit and premature differentiation into neuronal phenotypes.

Loss of *DENND5A* misorients mitotic spindles

When the zebrafish homolog of *PALS1* is depleted from the developing retina, progenitor cells undergo asymmetric oblique cell divisions rather than symmetric horizontal divisions, detach from the apical ventricular surface, and differentiate prematurely[24]. We performed a neural rosette formation assay, a polarized in vitro model of early neural development, to examine for potential alterations in the symmetry of cell division following loss of *DENND5A*. WT and *DENND5A* KO iPSCs were plated at low density in neural induction medium and neural rosettes were allowed to form for up to 7 days. After 1 day in vitro (DIV), both WT and KO rosettes had maximal OCT4 expression, a marker of pluripotency, which rapidly declined by DIV 3 and was completely abolished by DIV 5 (Supplementary Fig. 5a). Expression of the NPC marker SOX2 was observed after 1 DIV, reached maximal levels at DIV 3, then its expression was slightly reduced but stabilized at DIV 5–7 (Supplementary Fig. 5b). This characterization is in line with rosettes generated from both iPSCs and embryonic stem cells using various neural induction protocols[34,40,41]. In general, there were more rosettes formed per coverslip in WT cells compared to KO cells. As in the NPC proliferation experiment, this may be due to the large amount of cell death in the KO cells observed at DIV 1, reducing the number of stem cells initially available for rosette formation. WT rosettes were considerably denser than KOs, but rosette diameter, lumen area, and lumen perimeter did not differ significantly (Supplementary Fig. 5c-e). PALS1 localized apically in both WT and KO rosettes (Supplementary Fig. 5f), suggesting DENND5A is not involved in trafficking MUPP1/PALS1 to the apical membrane. However, the axis of cell division in relation to the lumen differed (Fig. 6a). Because F-actin accumulates apically during rosette formation[42] and outlines the cell borders of dividing cells, we used F-actin as a convenient marker of the apical surface. We measured the mitotic spindle angle, defined as the angle between the cleavage plane and the nearest apical surface, considering only cells with normally condensed chromatin and both centrosomes marked by γ-tubulin visible in the same plane. Although this exclusion criteria omitted many cells in WT rosettes dividing symmetrically along the z-plane or above the lumen (Supplementary Fig. 5g), as well as numerous observations of dividing cells with abnormally condensed chromatin in KO rosettes (Supplementary Fig. 5h), the spindle angle among cells dividing within WT ($M = 57.1°$, Mdn = 65.4°, SD = 25.9) and KO ($M = 26.0°$, Mdn = 20.1°, SD = 19.0) rosettes differed significantly according to a two-tailed Mann-Whitney U test ($Z = -7.122$, $p < 0.0001$;

Fig. 6b). An overwhelming majority of KO cells divided with spindle angles <45° (Fig. 6c), indicating that *DENND5A* KO results in increased levels of oblique asymmetric cell divisions and the ability for apical progenitors to self-renew is severely compromised.

A pool of DENND5A localizes to centrosomes

Due to their nucleation of astral microtubules of the mitotic spindle, which connect with the cell cortex and are the primary factor determining daughter cell positioning[43], alterations in cell division can result from changes in centrosome alignment. We hypothesized that because almost all dividing cells with normally condensed chromatin in *DENND5A* KO rosettes divided with a perpendicular orientation, centrosome dynamics promoting parallel, symmetric divisions were compromised. To gain insight into the subcellular function of DENND5A, we examined the localization of GFP-DENND5A WT or R710H in NPCs. In addition to a Golgi localization, which is consistent with previous studies[11], we identified that DENND5A also localized to γ-tubulin-positive centrosomes (Fig. 6d). No difference in localization was observed between WT and R710H constructs.

Discussion

Here we present a cohort of individuals with biallelic variants in *DENND5A* leading to a DEE on a spectrum of severity. When comparing the phenotype of the 2 cohort members exhibiting the most extensive neuroradiological phenotypes, some key similarities and differences between these individuals with *DENND5A*-DEE and other monogenic DEEs described in the literature can be noted. Although none of the neuroanatomical features that we report in *DENND5A*-DEE are unique to DEEs, we are unaware of any other monogenic DEE in the literature with patients that display the same combination of features as those observed in these most severe cases. There is a considerable degree of phenotypic overlap between these cases and a cohort comprised of individuals with pathogenic *PCDH12* variants, but the *PCDH12* patients lacked pachygyria and often co-presented with ophthalmic abnormalities, in contrast to what was observed here[44–46]. Cortical migration abnormalities and calcifications are observed in cases with recessive variants in the tight junction protein-encoding *OCLN* gene, but severe basal ganglia or diencephalic and mesencephalic dysplasias were not reported and polymicrogyria, a key feature of *OCLN* mutations, is not observed in our study[17]. Variants in tubulin genes also result in overlapping phenotypes[47], but our cases lack the classic dysgyria pattern and instead are observed in the context of occipital pachygyria and differ in that our cases are associated with calcifications. Moreover, it seems that our more severe cases have more extensive basal ganglia abnormalities when compared with the typical imaging presentations associated with *TUBA1A*, *TUBB2A*, *TUBB2B*, *TUBB3*, and *TUBG1*[48–51]. Variants in *LIS1*, encoding a protein involved in neuronal migration, results most frequently in a posterior gradient of lissencephaly, without calcifications, and variable degrees of corpus callosum size including thin, normal, and thicker than normal tracts[52]. In contrast, corpus callosum volumes were either normal, thin, or absent with no cases of increased volume in our cohort. Finally, there is a selective involvement of the cortex added to the presence of periventricular calcifications, a common association that brings cytomegalovirus-induced brain malformations into the differential but aligns with pseudo-TORCH syndrome diagnostic criteria in the absence of congenital infection[53,54]. However, due to a small cohort size, limited raw neuroimaging data, and reliance on incomplete clinical reports for some cases, we were unable to analyze all cases with a sufficient degree of detail to determine a genotype-phenotype relationship. Additionally, it appears that the radiological findings do not always correlate with disease severity, as seen in cases with severe developmental phenotypes but relatively mild neuroanatomical phenotypes. Nonetheless, our radiological findings combined with clinical information in Tables 1, 2 and Source Data provide physicians with valuable
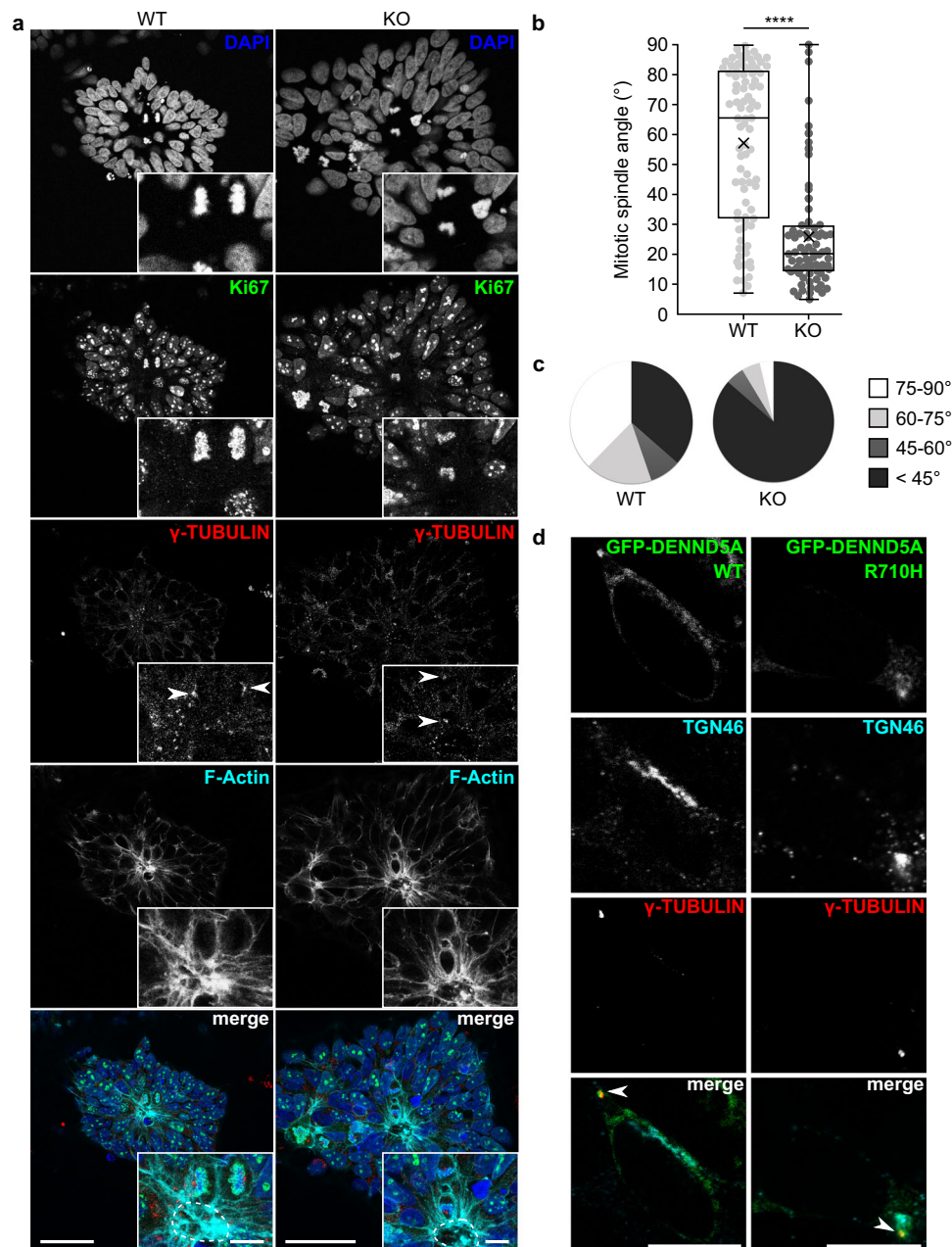
Fig. 6 | A neural rosette formation assay reveals abnormal mitotic spindle orientations upon loss of *DENND5A*. a Sample images showing the orientation of apical progenitor cell division in WT and *DENND5A* KO rosettes. Green = Ki67, red = γ-tubulin, cyan = F-actin, blue = DAPI. Scale bars = 50 μm, inset = 10 μm. Dotted lines outline the F-actin-positive lumen. **b** Quantification of mitotic spindle angles measured from n = 85 WT and n = 81 KO dividing cells from two independent experiments, analyzed via two-tailed Mann-Whitney U test (Z = −7.122, p = 1.07 × 10⁻¹²). **c** Pie charts showing the proportion of dividing cells with mitotic spindle angles falling within various ranges. **d** Overexpression of DENND5A in NPCs. Green = GFP-DENND5A, cyan = TGN46, red = γ-tubulin. Scale bars = 10 μm. Results were reproduced in two independent experiments. Source data for (**b**, **c**) are provided as a Source Data file.

information to communicate with families and treatment teams on a case-by-case basis.

For families in which one parent is aware they are a carrier of a pathogenic *DENND5A* variant, genetic counselors can recommend the other parent undergo genetic testing. When both parents are carriers, in vitro fertilization with preimplantation genetic diagnosis can be offered. However, the presence of *DENND5A* VUSs does not necessarily equate to a devastating prognosis; 13% (3 cases) of our small cohort did not meet criteria for DEE or experience seizures at the time of data collection. Detailed functional studies need to be performed to determine whether p.R1159W, p.P955L, p.T136R, and/or exon 1–14 duplication are pathogenic. Additionally, we believe American College

of Medical Genetics and Genomics classifications for several variants should be updated to pathogenic or likely pathogenic, especially p.R517W, p.K485E, p.D541G, and p.R710H, as these variants are found in individuals with brain abnormalities, severe intellectual disability, infantile seizure onset, and no other flagged gene variants. The identification of additional *DENND5A*-related DEE cases will prove valuable for future clinical and biological studies and thus improved treatment options and prognostic information for healthcare providers and families.

The identification of DENND5A as a polarity-related protein is consistent with previous clinical observations. Human cases with pathogenic variants in *CRB2* and *MUPP1* have been identified and

exhibit ventriculomegaly and corpus callosum dysgenesis[18,28,55–57], and patients with *PALS1* variants show global developmental delay, microcephaly, and sometimes seizures[19]. Moreover, the phenotypes observed in our *DENND5A*-related DEE mouse model overlap with those found in other mouse models targeting these proteins. *MUPP1* KO mice have enlarged lateral ventricles[30] and the cortex in *PALS1* conditional KO mice, where PALS1 was selectively depleted from cortical progenitors, fails to develop, leading to microcephaly[23]. The fact that the interaction between open DENND5A and MUPP1/PALS1 is weak may indicate that this occurs transiently in cells or only under specific circumstances. Indeed, the conformation-dependent nature of the interaction reflects the importance of these proteins remaining separate from each other under steady-state conditions and may reflect a molecular mechanism to regulate the balance of symmetric versus asymmetric cell division during mitosis. The biologically relevant mechanism for opening the DENND5A structure remains elusive, but possible candidates include posttranslational modifications or other currently unidentified protein-protein interactions. Future work should emphasize the mechanisms regulating the DENND5A conformational change and the role of its MUPP1/PALS1 interaction during cell division.

We have tested all commercial antibodies against DENND5A using several *DENND5A* KO cell lines and did not observe a specific signal via immunofluorescence, so the localization of endogenous DENND5A during cell division of apical progenitors is unknown. However, our expression studies indicate that a pool of DENND5A localizes to the centrosome in NPCs at interphase. No transfected cells in any other phase of the cell cycle were identified. One can speculate that DENND5A is involved in properly positioning centrosomes to align them parallel to the apical membrane during mitosis, ensuring that both daughter cells inherit apical determinants and remain in contact with the stem and progenitor cell biochemical niche found in the developing ventricle. This is indeed the case with the TJ and DEE-associated protein OCLN that binds directly to NuMa[21], which under normal circumstances coordinates with dynein and plasma membrane-associated proteins to tightly align the mitotic spindle through pulling forces and tethering astral microtubules to the cell cortex[58–63]. DENND5A may also play a role in core mitotic spindle assembly, as abnormal chromatin condensation was observed in many dividing *DENND5A* KO NPCs. However, the loss of parallel spindle orientation relative to the apical surface in virtually all remaining cells suggests a major function in astral microtubule tethering. Mora-Bermúdez et al. showed that a decrease in the number of molecules that link astral microtubules to the apical cell cortex leads to a decrease in the number of apicobasal-specific astral microtubules, resulting in a weakened anchor between the spindle poles and the apical cell cortex and promoting an oblique or perpendicular spindle orientation[64]. We, therefore, hypothesize that DENND5A functions in this capacity; that the centrosomal pool of DENND5A radiates outward as apicobasal astral microtubules nucleate to link them with MUPP1/PALS1 at the apical cell cortex, promoting a planar spindle orientation. Future studies could quantify the number of apicobasal astral microtubules in WT versus *DENND5A* KO dividing cells within rosettes to investigate this hypothesis.

Alternatively, or perhaps concurrently, DENND5A may regulate the inheritance of MUPP1 and PALS1 to maintain a neural stem cell identity. DENND5A is also a Golgi-localized protein (Fig. 6d and ref. 11) and the Golgi is confined to the apical process of apical progenitors in punctate stacks rather than a ribbon structure[65,66]. Golgi fragments containing DENND5A bound to PALS1/MUPP1 may thus ensure equal inheritance of apical determinants in both daughter cells of a dividing apical progenitor, affecting the resulting daughter cell fates.

Our study provides evidence for the involvement of *DENND5A* in two well-known processes implicated in primary microcephaly: centrosome positioning during cell division and premature NPC cell cycle exit and differentiation[67]. We propose a disease model, presented in Fig. 7, in which *DENND5A*-related DEE is driven by a significant reduction in symmetric cell divisions during early development due to the misorientation of cells away from the proliferative apical domain of the ventricular zone. This results in an imbalance of signaling molecules from the stem and progenitor cell niche to each daughter cell and unequal inheritance of apical determinants such as MUPP1 and PALS1, biasing one daughter cell toward a more fate-committed state[68]. Simultaneously, cells lacking functional DENND5A are inherently more likely to prematurely exit the cell cycle, further reducing the number of stem cells initially available during neurogenesis. Ultimately, this results in a shortened period of neurogenesis which leads to microcephaly and/or observable abnormalities in gray and white matter structures. The reduced volume of neurons likely leads to compensatory ventriculomegaly, and improperly positioned prematurely-born neurons that do not undergo apoptosis and form aberrant synaptic contacts results in seizures that can further adversely affect development.

Future experiments to strengthen this model could measure the mitotic spindle angle of dividing apical progenitors in the murine ventricular zone at various developmental timepoints to verify that daughter cells are indeed losing their contact with the stem cell niche as the rosette experiments suggest. Quantifying the proportions of stem cells and post-mitotic neurons in the embryonic VZ and SVZ will also provide valuable information; depending on the developmental timepoint that these cell division and differentiation abnormalities arise, these results would provide insight regarding the stem cell stage primarily affected (i.e., NECs versus aRG). Since DENND5A interacts with MUPP1, an apical protein that preferentially stabilizes AJs over TJs[27], and because unlike NECs, RG do not have TJs[33,69,70], we hypothesize that *DENND5A*-DEE is due to a defect in primarily aRG dynamics during development. Finally, further staining of the embryonic VZ and SVZ and the adult cortex for markers of progenitor and neuronal subpopulations will also expand the model, potentially providing clues for physicians to choose an antiseizure medication based on whether excitatory or inhibitory neurons are disproportionately affected.
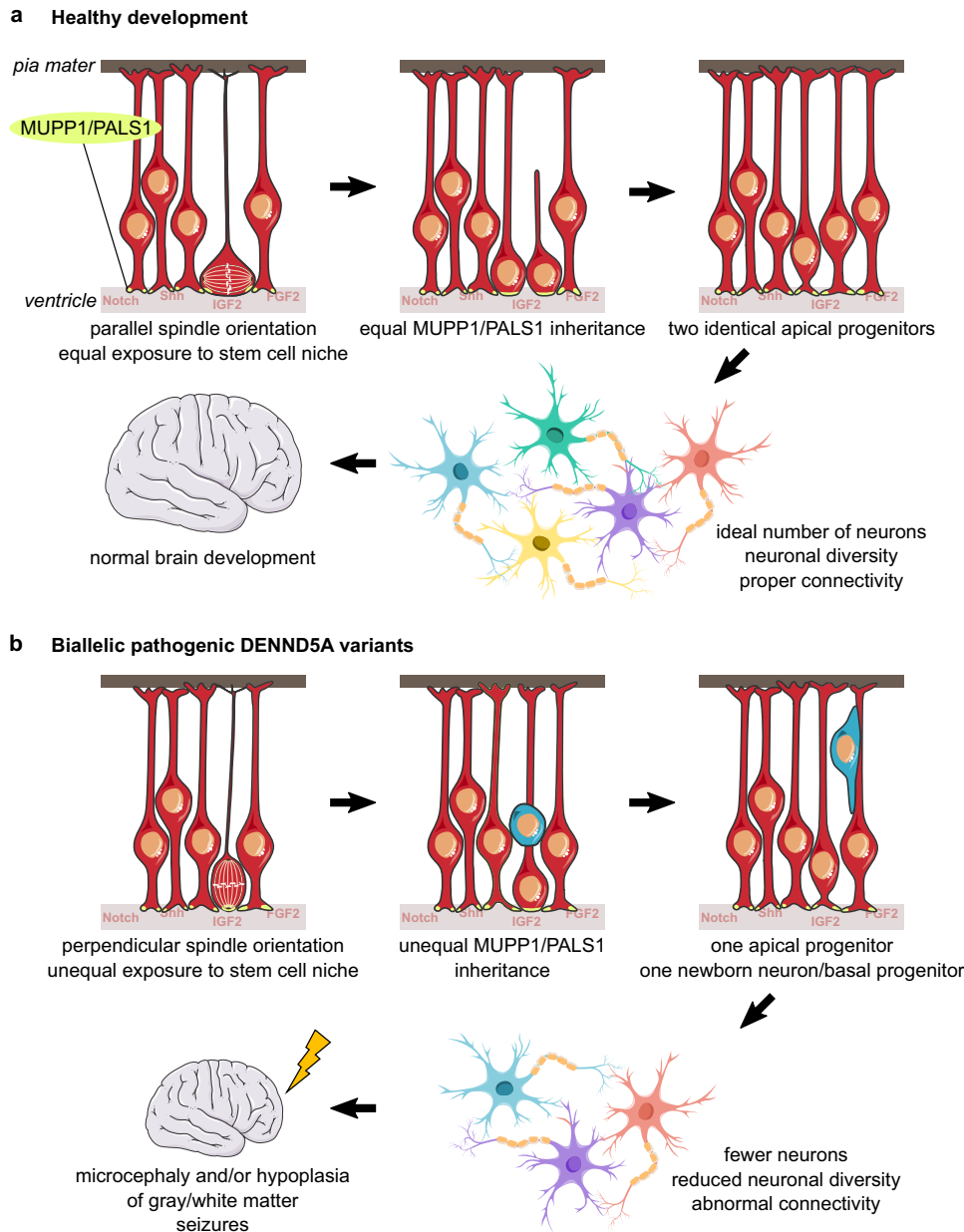
Methods

Participant recruitment

All materials and methods for participant recruitment and clinical data collection were approved by the McGill University Health Centre research ethics board (study 2021-6324) and the McGill Faculty of Medicine and Health Sciences institutional review board (study A12-M66-21B). All participants were recruited based on the presence of at least one variant in the gene *DENND5A*. Recruitment occurred through clinicians directly contacting our laboratory (16 participants) based on a previous publication about DENND5A[2] (4 participants), through GeneMatcher[71] or ClinVar[72] genetic databases (5), through contacting corresponding authors of other publications that briefly described patients with DENND5A variants[3] (2), and through word-of-mouth between collaborators of our study (3). Sex and gender were not considered in study design, and the research findings do not apply to only one sex. Pathogenic variants, likely pathogenic variants, and variants of unknown clinical significance were all eligible for inclusion in the study. Six individuals were ineligible and were excluded from analysis: two participants were heterozygous for a *DENND5A* variant, one was excluded due to death occurring prior to clinical data collection[2], and three were excluded because the questionnaires were not returned. Recruitment spanned approximately four years.

Phenotypic data collection and analysis

Clinicians with patients harboring biallelic *DENND5A* variants completed an anonymized phenotypic questionnaire based on their patient's most recent clinic visits. Available anonymized MRIs, CTs, and/or or official reports were contributed if the patient underwent

a   Healthy development

parallel spindle orientation
equal exposure to stem cell niche

equal MUPP1/PALS1 inheritance

two identical apical progenitors

ideal number of neurons
neuronal diversity
proper connectivity

normal brain development

b   Biallelic pathogenic DENND5A variants

perpendicular spindle orientation
unequal exposure to stem cell niche

unequal MUPP1/PALS1
inheritance

one apical progenitor
one newborn neuron/basal progenitor

fewer neurons
reduced neuronal diversity
abnormal connectivity

microcephaly and/or hypoplasia
of gray/white matter
seizures

Fig. 7 | DENND5A-related DEE disease model. a Under healthy developmental circumstances, apical progenitors are able to obtain a spindle orientation parallel to the apical ventricular surface. This allows both daughter cells to receive equal exposure to the stem and progenitor cell niche as well as inherit equal proportions of apical determinants, such as MUPP1 and PALS1, producing two identical apical progenitors after mitosis. The expansion of the progenitor pool early in brain development allows for an ideal production of neurons from diverse lineages and contributes to healthy brain development. **b** In the presence of biallelic pathogenic DENND5A variants, apical progenitors increasingly divide with a spindle angle perpendicular to the ventricular surface. This scenario only allows for one daughter cell to receive signaling molecules from the stem and progenitor cell niche and to inherit apical determinants, and the more basal daughter cell becomes either a basal progenitor or an immature neuron. Increased asymmetric cell division of apical neural progenitors during early development reduces the number of progenitors available for neurogenesis, resulting in a decreased overall number and diversity of neurons that contribute to microcephaly. This may contribute to abnormal neuronal connectivity, resulting in seizures that further adversely affect development, leading to DEE.

neuroimaging for clinical purposes. Participants were assigned a numerical ID in the order in which their questionnaires were received. For intronic variant analysis, molecular consequences were predicted using Ensembl's Variant Effect Predictor[73]. For those whose raw MRI or CT data were provided, an independent neuroradiologist re-analyzed the scans and completed the "Brain" section of the questionnaire without viewing the original submitted questionnaires. If responses to an item differed between the original clinician and the independent radiologist, the independent radiologist's response was used for analysis. Data are missing if the presence of a phenotype is officially

unknown. The most frequently reported phenotypes (present in >50% of the cohort) were arranged into a Venn diagram using an online tool (https://www.meta-chart.com) to illustrate the degree of phenotypic overlap within and between participants. For occipitofrontal circumference (OFC), if percentiles were not given directly from clinicians, percentile values were derived from the age- and sex-appropriate Word Health Organization tables (https://www.who.int/tools/child-growth-standards/standards/head-circumference-for-age). The OFC percentile for one person whose measurements were taken when they were above 5 years old was derived from tables published in

ref. 74. For calculating central tendency statistics, OFC percentiles given as a range (e.g., <3 or <1) were assigned a conservative numerical estimate (e.g., 2.9 for <3, 0.9 for <1). For phenotype severity quantification, the presence or absence of motor skills or abnormalities, neurological abnormalities, communicative abilities, motor skills, and medical or psychiatric comorbidities were compared in a systematic way across the group to allow for direct comparison (see Supplementary Methods in the Supplementary Information file for scoring tables).

Establishment of cell lines

The control hiPSC line AIW001-02 was derived from peripheral blood mononuclear cells of a healthy female donor (Caucasian, 48 years old) with informed consent under the McGill University Health Center Research Ethics Board project DURCAN_IPSC/2019-5374. The AIW001-02 cell line was generated by using the CytoTune™-iPS 2.0 Sendai Reprogramming Kit (iPSQuebec Platform, Laval University) and functionally characterized as described previously[75]. For knockout of human *DENND5A*, guide RNAs (gRNAs) were designed using an online tool (https://benchling.com). Both gRNA target sites are on *DENND5A* exon 4. Synthesized gRNAs were ordered from SYNTHEGO and transfection was performed following the manufacturer's protocol. Single-cell colonies were picked and amplified. Genomic DNA from the colonies was extracted with QuickExtract (Lucigen) and PCR was performed using Q5 High-Fidelity DNA Polymerase according to the manufacturer's protocol (F: GAGGATCGCCAGTGAGTGTT; R: CCCCGAGCAGTTCAAAAACC). A 238 base pair deletion was confirmed by Sanger sequencing, and AIW001-02 *DENND5A* KO iPSCs were functionally validated using the same characterization protocol[75].

Human fibroblasts from DENND5A cohort members were obtained with informed consent (DURCAN_IPSC/2019-5374) by skin biopsy (participants 2 and 10) and renal epithelial cells from a urine sample (participant 3). Cells were reprogrammed to hiPSCs by electroporation with episomal plasmids (pCXLE-hUL, pCXLE-hSK, and pCXLE-hOCT4) as previously described[76]. Generated hiPSCs were functionally and genomically validated according to Hauser and Erzler[77].

Lymphoblasts were obtained from a healthy individual (control line) and two homozygous individuals (participants 4 and 5) followed by immortalization through the use of the Epstein-Barr virus in the lab of Dr. Fowzan Alkuraya. Informed consent was obtained to both collect the samples and share them with external researchers under the researchers' local IRB (KFSHRC RAC #2080 006).

Cell culture

hiPSCs were cultured on hESC-qualified Corning Matrigel-coated tissue culture dishes in either TeSR-E8 medium (all patient-derived iPSC lines; STEMCELL Technologies) or mTeSR1 medium (AIW001-02 WT and *DENND5A* KO; STEMCELL Technologies) with daily medium changes and mechanical removal of differentiated cells. Cells were passaged using the ReLeSR Passaging Reagent (STEMCELL Technologies) once cultures reached approximately 70% confluency.

hiPSCs were differentiated to NPCs using the STEMdiff SMADi Neural Induction Kit (STEMCELL Technologies) with daily medium changes. Induced cultures were passaged using Accumax (Millipore Sigma) once cells reached 90-95% confluency, approximately once per week. After a 2-week induction period, NPCs were maintained in STEMdiff Neural Progenitor Medium (STEMCELL Technologies) on poly L ornithine (PLO)- and laminin-coated plates and passaged using Accumax once cultures reached 90–95% confluency, approximately once per week. Experiments examining β-III tubulin expression examined established NPC lines after one passage post-neural induction; all other experiments were performed using cells at passages 2–4.

Control and patient-derived Epstein-Barr virus-induced lymphoblastoid cell lines were obtained from the laboratory of Dr. Alkuraya. Cells were cultured in suspension in RPMI 1640 medium (Gibco)

supplemented with 15% fetal bovine serum (Wisent), 1% penicillin-streptomycin (Wisent), and 1% L-glutamine (Wisent). Cells were split 1:4 once confluency reached approximately 1×10^6 cells/ml.

For biochemical studies, HEK293-T cells were cultured in DMEM high glucose (Fisher) supplemented with 10% bovine calf serum (Fisher), 1% L-glutamine (Wisent), and 1% penicillin-streptomycin (Wisent).

Because this autosomal recessive disease appears to affect males and females approximately equally, sex was not considered in study design when conducting in vitro experiments.

Plasmid cloning

DENND5A cDNA (Origene, SC121400) was cloned into the pCMV-tag2B vector to generate FLAG-DENND5A. GFP-DENND5A was made via subcloning DENND5A into the pEGFP-C1 vector. Patient variants and targeted residues for biochemical studies were introduced using the QuikChange Lightning site-directed mutagenesis kit (Agilent) following the manufacturer's protocol. FLAG-DENND5A DENN domain was made by subcloning aa1-680 of DENND5A into the pCMV-tag2B vector. GST-aa700-720 was made via oligo annealing followed by ligation into a pGEX-4T1 vector with a modified multiple cloning site (MCS). GST-RUN1/PLAT was created by subcloning DENND5A aa707-1090 into the pGEX-6P1 vector. MUPP1 (MPDZ) was obtained from the Harvard Medical School plasmid collection (HsCD00352820). pDONR223-MPP5 was a gift from William Hahn & David Root (Addgene plasmid # 23447; http://n2t.net/addgene:23447; RRID:Addgene_23447)[78] and subcloned into a pCMV3-C-FLAG vector to generate PALS1-FLAG. The vector backbone from PALS1-FLAG was then isolated and modified to include a custom MCS via oligo annealing and ligation in order to create restriction sites suitable for subcloning MUPP1 into the vector. MUPP1 was subcloned into this modified vector to create MUPP1-FLAG. All constructs were confirmed by Sanger sequencing.

RT-qPCR

RNA was extracted from NPCs and lymphocytes using the RNeasy kit (Qiagen) followed by cDNA synthesis using iScript Reverse Transcription Supermix for RT-qPCR (Bio-Rad). RT-qPCR was performed using SsoFast EvaGreen Supermix (Bio-Rad) with primers targeting human *DENND5A* (F: CTAAAGCCAGGGATGGTGCC; R: TTTCGGCATACATAGCATTCCT) and *TBP* (F: TGCACAGGAGCCAAGAGTGAA; R: CACATCACAGCTCCCCACCA). *DENND5A* levels were normalized to *TBP* levels and AIW001-02 WT NPCs or control lymphocytes.

RNA from mouse brain tissue was extracted using RNeasy Lipid Tissue kit (Qiagen), followed by cDNA synthesis and RT-qPCR performed with the same reagents as above using primers specific to the mouse genome for *DENND5A* (F: CAGTCGCTTCGCCGACTAT; R: GCACCATCCCTGGCTTTAGAA) and *GAPDH* (F: ACTCCACTCACGGCAAATTC; R: CCAGTAGACTCCACGACATACT). *DENND5A* levels were normalized to *GAPDH* levels in WT mice.

RNA was extracted from zebrafish samples using TRIzol Reagent (Thermo Fisher Scientific) and purified with the RNA Clean and Concentrator-5 kit (Zymo Research) according to the manufacturer's guidelines. cDNA was synthesized using iScript Reverse Transcription Supermix (Bio-Rad). RT-qPCR was performed on the Light Cycler 96 System (Roche) using specific primers for zebrafish *dennd5a* (F: TTGGCGAGTGCAAATGAAGG; R: GTTTGCTGGTCACCTCCTCA) along with SYBR Green Supermix (Thermo Fisher Scientific). *dennd5a* expression levels were normalized to the *18S* gene (F: TCGCTAGTTGGCATCGTTTATG; R: CGGAGGTTCGAAGACGATCA) and the 1 hpf stage (in temporal *dennd5a* expression analysis) or to Cas9-injected control animals (to analyze *dennd5a* expression in control versus F_0 KO animals).

Neural rosette formation assay

hiPSCs were gently dissociated into a single cell suspension and plated at low density (20,000 cells per well of a 24-well plate) onto PLO/

Laminin-coated coverslips in neural induction media with SMAD inhibitor (STEMCELL Technologies #08581) containing 10 μM Y-27632 on the day of plating. Medium was changed daily and cells were fixed after 1, 3, 5, and 7 days in culture. Rosettes were stained and z-stack images in 0.5 μm increments were taken using the Leica SP8 confocal microscope. For lumen size analysis, z-plane images with the largest visible lumens were used for quantification followed by two-tailed Mann-Whitney U tests. For rosette diameter analysis, z-plane images with the widest phalloidin staining were used for quantification followed by a two-tailed student's *t*-test. To analyze dividing cells within the rosettes, cells in metaphase, anaphase, and telophase were used for quantification. Mitotic spindle angles were measured as in ref. [79] using F-actin as a marker of the apical surface and quantified using ImageJ.

Immunocytochemistry
Samples were fixed in 4% paraformaldehyde for 20 min at room temperature. Cells were permeabilized for 5 min in 0.1% Triton-X 100 and then blocked in 5% BSA and 0.01% Triton-X 100 in PBS for 30 min at room temperature, followed by overnight incubation at 4 °C with the following antibodies: OCT4 (ab19857, 1 μg/ml), SOX1 (Invitrogen MA5-32447, 1:200), SOX2 (Abcam ab92494, 1:1000), Nestin (Invitrogen, MA1-110, 1:100), β-III tubulin (Abcam ab52623, 0.1 μg/ml), Ki67 (Abcam ab15580, 0.5 μg/ml), γ-tubulin (Sigma-Aldrich T6557, 1:500), and Pals1 (Santa Cruz Biotechnology sc-365411, 1:350). After primary antibody incubation, samples were washed twice with PBS then incubated with Alexa-conjugated secondary antibodies at 1:500 dilution and phalloidin at 1:1000 dilution for 1 h at room temperature. Cells were then washed twice in PBS, incubated with DAPI at 1:5000 dilution for 10 min, washed twice in PBS again, and mounted onto glass slides.

Endogenous and transfected protein expression
NPCs were harvested in RIPA buffer adjusted to pH 7.4 (50 mM Tris pH 7.4, 150 mM NaCl, 1 mM EDTA pH 8, 1% sodium deoxycholate, 0.1% SDS, 1 mM DTT, 0.83 mM benzamidine, 0.5 μg/ml aprotinin, 0.5 g/ml leupeptin, 0.23 mM phenylmethylsulfonyl fluoride) followed by incubation with 1% Triton X-100 for 15 min and centrifugation at 21,100 × g for 15 min at 4 °C. Lymphoblasts were harvested in lysis buffer (20 mM HEPES pH 7.4, 100 mM NaCl, 0.83 mM benzamidine, 0.5 μg/ml aprotinin, 0.5 g/ml leupeptin, 0.23 mM phenylmethylsulfonyl fluoride) containing 1X LSB. Mouse brains were homogenized in lysis buffer and incubated with 1% Triton X-100 for 15 min at 4 °C, followed by centrifugation at 239,000 × g for 15 min at 4 °C. For FLAG-DENND5A expression, plasmid DNA was transfected into HEK293T cells using the calcium phosphate method and cells were harvested after 24 h in lysis buffer containing 1X LSB. Equal protein aliquots were loaded onto an SDS-PAGE gel and analyzed via Western blot using primary antibodies against DENND5A (ThermoFisher #702789, 2.5 μg/ml), FLAG (clone M2, Sigma-Aldrich, 1:10,000), Hsc70 (clone 1B5, StressGen Biotechnologies Corp, 1:1:10,000), and β-actin (Clone C4, Sigma-Aldrich MAB1501R, 1:1000).

Pulldown experiments
500 mL flasks of bacteria were induced overnight at RT to express GST-tagged proteins using 500 μM IPTG when the optical density of the cultures at 600 nm reached 0.6. Bacteria were pelleted and resuspended in PBS + protease inhibitors pH 7.4. Resuspended bacterial cells were then sonicated three times for 5 s at 70% amplitude, followed by incubation with 1% Triton X-100 for 15 min. The bacterial cell lysate was then spun for 5 min at 4 °C at 11,952 × g. The supernatant was incubated with glutathione Sepharose beads, pre-washed three times in PBS, for 1 h at 4 °C, and beads were then briefly spun down and washed three times in PBS + protease inhibitors to purify GST fusion proteins. The concentration of fusion proteins was determined by running on an SDS-PAGE gel accompanied by a BSA standard curve

followed by Coomassie Brilliant Blue staining. Cell lysates were then harvested for incubation with GST fusion proteins.

For pulldown experiments with overexpressed proteins, HEK293-T cells were transfected using the calcium phosphate method with the appropriate plasmids and harvested the next day in lysis buffer. Cells were then sonicated once for 10 s at 20% amplitude, incubated in 1% Triton X-100 for 15 min at 4 °C, and spun at 21 × g and 4 °C for 15 min in a tabletop centrifuge. The concentration of HEK293T supernatants was analyzed via a Bradford assay, and 1 mg/ml was incubated with 20 μg (GST-aa700-720) or 100 μg (GST-RUN1/PLAT) of fusion proteins for one hour at 4 °C. Following incubation, beads were washed 3 times in buffer containing 1% Triton, eluted in 1X LSB, loaded onto an SDS-PAGE gel, and analyzed via Western blot using primary antibodies against FLAG (clone M2, Sigma-Aldrich, 1:10,000).

Mass spectrometry
For the initial protein-protein interaction screen followed by mass spectrometry, 4 E18 rat brains were homogenized on ice in 1 ml lysis buffer per brain (20 mM HEPES pH 7.4, 150 mM NaCl, 0.83 mM benzamidine, 0.5 μg/ml aprotinin, 0.5 μg/ml leupeptin, and 0.23 mM phenylmethylsulfonyl fluoride) with 10 strokes using a Caframo homogenizer at 1200 rpm. Tissue homogenate was then sonicated once for 10 s at 20% amplitude, incubated in 1% Triton X-100 for 15 min at 4 °C, and spun at 239,000 × g and 4 °C for 15 min. Supernatant concentration was determined via a Bradford assay and 1 mg/ml was incubated with 50 μg GST-fusion protein overnight at 4 °C. Following incubation, beads were washed 3 times in lysis buffer containing 1% Triton, then eluted in 1X LSB.

For each sample, proteins were loaded onto a single stacking gel band to remove lipids, detergents, and salts. The gel band was reduced with DTT, alkylated with iodoacetic acid, and digested with Trypsin. Extracted peptides were re-solubilized in 0.1% aqueous formic acid and loaded onto a Thermo Acclaim Pepmap (Thermo, 75 μM ID × 2 cm C18 3 μM beads) precolumn and then onto an Acclaim Pepmap Easyspray (Thermo, 75 μM × 15 cm with 2 μM C18 beads) analytical column separation using a Dionex Ultimate 3000 uHPLC at 250 nl/min with a gradient of 2–35% organic (0.1% formic acid in acetonitrile) over 2 h. Peptides were analyzed using a Thermo Orbitrap Fusion mass spectrometer operating at 120,000 resolution (FWHM in MS1) with HCD sequencing (15,000 resolution) at top speed for all peptides with a charge of 2+ or greater. The raw data were converted into *.mgf format (Mascot generic format) for searching using the Mascot 2.6.2 search engine (Matrix Science) against all rat protein sequences (Uniprot 2017). Search parameters for peptides >5 residues were ±5 ppm on the parent ion and 0.1 amu on fragment ions. A fixed modification for carboxymethyl-Cysteine was used along with variable modifications of Oxidation (methionine) and deamination (asparagine/glutamine). At 99.0% protein and 95% peptide confidence, 1077 proteins (34,443 spectra) were identified using 1 peptide (0.0% peptide FDR and 0.40% protein FDR). The database search results were loaded onto Scaffold Q+ Scaffold_4.8.6 (Proteome Sciences) for statistical treatment and data visualization.

Co-immunoprecipitation experiments
For co-immunoprecipitation experiments, HEK293-T cells were transfected using the calcium phosphate method, harvested in lysis buffer, and sonicated once for 10 s at 20% amplitude, followed by incubation in 0.5% Triton X-100 for 15 min at 4 °C. Cell lysate was then spun at 21 × g and 4 °C for 15 min in a tabletop centrifuge, and 1 mg/ml of the resulting supernatant was incubated for one hour at 4 °C with 25 μl ChromoTek GFP-Trap Agarose magnetic beads pre-equilibrated three times in lysis buffer without Triton X-100. Beads were then washed three times in lysis buffer containing 0.05% Triton and then eluted in 1X LSB for SDS-PAGE analysis and analyzed via Western blot using

primary antibodies against FLAG (clone M2, Sigma-Aldrich, 1:10,000) and GFP (Invitrogen Cat# A-6455, 1:20,000).

Animal care and selection

All mouse care and experiments in the study were approved by the Montreal Neurological Institute Animal Care Committee in accordance with guidelines set by the Canadian Council on Animal Care under ethical protocol number 5734. The experimental unit for this study is a single animal. Apart from selecting animals based on *DENND5A* genotype, no exclusion criteria were set for the experiments. Sex was not considered in the study design because there is an approximately equal distribution of males and females in the human cohort, so both male and female animals were used.

Crispant zebrafish experiments used wild-type strain NHGRI-1[80] according to the protocol approved by the Institutional Animal Care Committee of Oklahoma Medical Research Foundation (22-18). All animals were raised and maintained in an Association for Assessment and Accreditation of Laboratory Animal Care accredited facility under standard conditions.

Establishment of transgenic animal models

KI mice were generated by the McGill Integrated Core for Animal Modeling. Two silent mutations were introduced in L168 and L169 (CTTGCT –>TTAGCA) as well as a deletion of 2 bp in G172 to introduce a frameshift and premature stop codon in exon 4 of the *DENND5A* mouse gene. Briefly, custom sgRNAs (CTTCATGCTCCACTTGCT-GATGG, Synthego), Cas9 protein (IDT, Cat#1081058) and ssODN (ultramer, IDT) were microinjected into the pronucleus of C57BL/6 N mouse zygotes with concentrations of 50:50:30 ng/µl respectively. Embryos were subsequently implanted in CD-1 pseudopregnant surrogate mothers according to standard procedures approved by the McGill University Animal Care Committee. Founder pups (F0) were genotyped for evidence of deletion of 2 bp in G172 and mated to wild-type C57BL/6N (Charles River) mice for three generations. The colony was maintained by sibling mating and by crosses to C57BL/6N mice every third generation. All genomic sequencing was performed using the Big Dye Terminator Ready Reaction Mix (ABI, Carlsbad, CA, USA) at the McGill and Genome Quebec Innovation Center (Primers: ACAAG-GAATGCTCTCACTGC, CACACTCCGACATGCCTTCAT [417 bp]). Obtained sequences were analyzed using an online tool (https://benchling.com).

Previously described methods were used to generate *dennd5a* KO zebrafish in crispant experiments[81,82] using single-guide RNAs (sgRNAs) designed using the CRISPOR tool targeting three *dennd5a* sites (GGTGTTTGAGCTGCTAGGGC, GGGCTGATCTGACAGGAAGG, AGATG GGCCATGATAACTCA) and synthesized by in vitro transcription. Embryos at the one-cell stage were injected with a mixture containing Cas9 protein with (F0 knockouts) or without (control) sgRNAs.

4-aminopyridine-induced seizure assay

6-month-old mice ($M = 183.9$ days, $SD = 1.0$) were injected with the K+ channel blocker 4-aminopyridine (8 mg/kg, i.p.) (Sigma-Aldrich, Canada) to induce seizures. If no seizures were observed after 30 min, they were re-injected with a half-dose of 4-aminopyrdine (4 mg/kg, i.p.). Animals that showed no seizures after the second dose were excluded from further analysis. Seizures were identified based on behavioral symptoms such as myoclonic activity of rear and forelimbs that evolved to rearing and loss of balance. The latency (min) from the time of the last 4-aminopyridine injection and seizure onset was calculated.

Zebrafish morphological and behavioral phenotyping

Morphological phenotyping was conducted by randomly selecting Cas9-injected control and F0 KO animals at 5 days post fertilization (dpf) and anaesthetizing them with Tricaine/MS-222 (Sigma-Aldrich).

The animals were positioned in 2% methylcellulose (Sigma Aldrich) under a stereomicroscope and imaged using a high-definition Nikon DS-Fi2 camera mounted on a Nikon SMZ18 stereomicroscope. Head and eye sizes were measured from scale-calibrated images using ImageJ.

All behavioral tests were conducted at room temperature. Acoustically evoked behavioral response tests were carried out using Zebrabox behavior chambers (Viewpoint Life Sciences) as previously described[82] involving the percentage of responses for 12 stimuli per larva. The visual startle response test was performed using the DanioVision system running EthoVision XT software (Noldus Information Technology, Leesburg), as previously reported[82,83] based on the number of responses for five stimuli per larva. For locomotor behavior recording during light/dark transitions, 4 dpf larvae were transferred to a 96-well plate, with one larva per well in 150 µL of embryo water. The following day, the plate was placed in a Noldus chamber, and the DanioVision system running EthoVision XT software was used to record locomotion activity. The 5 dpf larvae underwent a 30-minute habituation period in the light, followed by three cycles of 10-min light and 10-min dark transitions. The locomotion activity of the larvae was recorded as the distance traveled in millimeters (mm) per minute.

Whole-mount in situ hybridization (WISH)

WISH was performed on zebrafish embryos using a previously described method[84] using a 673-bp amplicon of zebrafish dennd5a cDNA produced via PCR (Primers: T3-dennd5a_F: gaatt-gaattaaccctcactaaagggCGAGTGCAAATGAAGGTGAG; T7-dennd5a_R: gaattgtaatacgactcactatagggGGTCTCTGACAGATCACTGG).

Immunohistochemistry

Mouse brain sections from 124-day-old mice were baked overnight at 60 °C in a conventional oven. Samples were then deparaffinized and rehydrated in a series of xylene and ethanol washes, followed by antigen retrieval using citrate buffer (pH 6.0) for 10 min at 120 °C in a decloaking chamber (Biocare Medical). Slides were then rinsed with IHC buffer (PBS + 0.05% Tween-20 + 0.2% Triton X-100) and blocked for 1 h with Protein Block (Spring Bioscience), incubated with primary antibodies overnight at 4 °C, and washed with IHC buffer followed by incubation with respective secondary antibodies (Invitrogen) for 1 h at room temperature. Coverslip mounting was done using ProLong Diamond Gold Antifade Mountant with DAPI (Invitrogen) to stain nuclei. Images were acquired using Leica SP8 laser scanning confocal microscope. Quantification of the percentage of cells per mm^2 labeled by NeuN or GFAP was based on three 10x magnification images per animal from a total of $n = 4$ mice. Cells within 100 µm of the ependymal layer (excluding the ependymal cells) in which DAPI signal was also evident were considered. All measurements were done using ImageJ.

For zebrafish, 6 dpf larvae were first blocked in blocking buffer (10 % Goat Serum, 1% BSA, 1% DMSO and 0.5 % Triton X-100 in PBS) overnight at 4 °C, followed by incubation with primary antibodies, including mouse IgG2b anti-acetylated tubulin (1:200; Sigma-Aldrich) and anti-SV2 (1:200; DSHB), for 5 days with gentle agitation in a cold room. After washing 3 times with PBSTx, larvae were incubated with secondary antibodies, including goat anti-rabbit IgG Alexa Fluor 488 (1:500, Jackson ImmunoResearch) and goat anti-mouse IgG Alexa Fluor 647 antibody (1:500, Jackson ImmunoResearch, PA) for 3 days at 4 °C. Following a series of washes, larvae were laterally mounted in 1.5% low melting point agarose (Sigma-Aldrich), and images were obtained using the Zeiss LSM-710 Confocal microscope.

7 T small animal MRI

Ten WT (3 males, 7 females, mean age = 114 days, SD = 12.9) and 10 KI (3 males, 7 females, mean age = 108 days, $SD = 10.3$) for a total of 20 mice

were employed for high resolution, pre-clinical MR imaging experiments. Data from four animals were excluded from analysis to restrict subjects to an age range of ~3–4 months for consistency. For in vivo structural MRI, mice were anesthetized with isoflurane, placed in a plastic bed and restrained with gauze pads to minimize the possible influence of motion artifacts. For the duration of each MRI scan, mice were maintained under isoflurane gas anesthesia at approximately 37 °C using a warm air blower and respiration was monitored using a pressure pad.

Imaging was performed using the 7 T Bruker Pharmascan (Bruker Biosciences, Billerica, MA), ultra-high field, pre-clinical MRI system of the McConnell Brain Imaging Centre at McGill University. The Pharmascan is equipped with an AVANCE II-model spectrometer and BFG-150/90-S shielded gradient system (Resonance Research Inc., Billerica, Massachusetts). Structural MR images were acquired using a 2D Rapid Imaging with Refocused Echoes (RARE) pulse sequence with the following parameters: effective echo time (TE_{eff}): 30 ms, RARE factor: 8. In-plane resolution: $100 \,\mu m \times 100 \,\mu m$, slice thickness: $300 \,\mu m$ and receiver bandwidth: 46,875 Hz. The repetition time (TR) and the number of acquired slices were varied for two pairs of WT/KI mice in order to achieve greater slice coverage along the rostro-caudal axis (TR: 4000 ms to 4750 ms, number of slices: 40–50). The number of averages was varied to optimize total scan time for mouse imaging under gas anesthesia. Lateral ventricles were manually segmented in each scan by a researcher blind to animal genotypes using the ITK-SNAP software (www.itksnap.org)[85]. and pooled lateral ventricle volumes were used for statistical analysis.

Statistics and reproducibility
Continuous data were analyzed for normality and homogeneity of variance using Shapiro-Wilk tests ($n < 50$) or Kolmogorov-Smirnov ($n \geq 50$) tests and Levene tests. Student's t tests or one-way ANOVAs were conducted when all assumptions were met. Welch's t-tests were conducted when homogeneity of variance assumptions was not met. The nonparametric equivalent (Mann-Whitney U test) was conducted when normality assumptions were not met, or when both normality of data and homogeneity of variance assumptions were not met. Data were analyzed using SPSS, R version 4.1.2 with Companion to Applied Regression package version 3.0, and Tidyverse version 1.3.1 software. All statistical analyses included multiple replicates from several independent experiments. A p value of <0.05 was considered statistically significant. Asterisks in figures represent p values: * = $p < 0.05$, ** = $p \leq 0.01$, *** = $p \leq 0.001$, **** = $p \leq 0.0001$. Box plots in figures are defined as follows: whiskers = minima and maxima, X = mean, horizontal line = median, bounds of the box indicate the interquartile range, and each dot represents one individual data point.

Reporting summary
Further information on research design is available in the Nature Portfolio Reporting Summary linked to this article.

Data availability
The mass spectrometry proteomics data have been deposited to the ProteomeXchange Consortium via the PRIDE[86] partner repository with the dataset identifier PXD048699. The clinical phenotyping, animal phenotyping, RT-qPCR, uncropped blots, and quantitative in vitro and ex vivo data generated in this study are provided in the Supplementary Information/Source Data file. Data concerning in vitro experiments and in vivo and ex vivo mouse experiments were generated at the Neuro of McGill University. Data concerning zebrafish experiments were generated at the Oklahoma Medical Research Foundation. Derived data supporting any other findings of this study are available upon reasonable request from the corresponding author. Source data are provided with this paper.

References
1. Raga, S., Specchio, N., Rheims, S. & Wilmshurst, J. M. Developmental and epileptic encephalopathies: recognition and approaches to care. *Epileptic Disord.* **23**, 40–52 (2021).
2. Han, C. et al. Epileptic encephalopathy caused by mutations in the guanine nucleotide exchange factor DENND5A. *Am. J. Hum. Genet.* **99**, 1359–1367 (2016).
3. Anazi, S. et al. Clinical genomics expands the morbid genome of intellectual disability and offers a high diagnostic yield. *Mol. Psychiatry* **22**, 615–624 (2017).
4. Marat, A. L., Dokainish, H. & McPherson, P. S. DENN domain proteins: regulators of Rab GTPases. *J. Biol. Chem.* **286**, 13791–13800 (2011).
5. Callebaut, I., de Gunzburg, J., Goud, B. & Mornon, J. P. RUN domains: a new family of domains involved in Ras-like GTPase signaling. *Trends Biochem. Sci.* **26**, 79–83 (2001).
6. Janoueix-Lerosey, I., Jollivet, F., Camonis, J., Marche, P. N. & Goud, B. Two-hybrid system screen with the small GTP-binding protein Rab6. Identification of a novel mouse GDP dissociation inhibitor isoform and two other potential partners of Rab6. *J. Biol. Chem.* **270**, 14801–14808 (1995).
7. Recacha, R. et al. Structural basis for recruitment of Rab6-interacting protein 1 to Golgi via a RUN domain. *Structure* **17**, 21–30 (2009).
8. Fernandes, H., Franklin, E. & Khan, A. R. Crystallization of an engineered RUN domain of Rab6-interacting protein 1/DENND5. *Acta Crystallogr. Sect. F. Struct. Biol. Cryst. Commun.* **67**, 556–560 (2011).
9. Fernandes, H., Franklin, E., Jollivet, F., Bliedtner, K. & Khan, A. R. Mapping the interactions between a RUN domain from DENND5/Rab6IP1 and sorting nexin 1. *PLoS One* **7**, e35637 (2012).
10. Wassmer, T. et al. The retromer coat complex coordinates endosomal sorting and dynein-mediated transport, with carrier recognition by the trans-Golgi network. *Dev. Cell* **17**, 110–122 (2009).
11. Miserey-Lenkei, S. et al. Rab6-interacting protein 1 links Rab6 and Rab11 function. *Traffic* **8**, 1385–1403 (2007).
12. Li, Y. et al. Cancer driver candidate genes AVL9, DENND5A and NUPL1 contribute to MDCK cystogenesis. *Oncoscience* **1**, 854–865 (2014).
13. Yang, M. et al. Novel loss-of-function variant in DENND5A impedes melanosomal cargo transport and predisposes to familial cutaneous melanoma. *Genet. Med.* **24**, 157–169 (2022).
14. Navis A., Bagnat, M. *Apicobasal Polarity and Lumen Formation During Development* (Springer, 2015).
15. Lamus, F. et al. FGF2/EGF contributes to brain neuroepithelial precursor proliferation and neurogenesis in rat embryos: the involvement of embryonic cerebrospinal fluid. *Dev. Dyn.* **249**, 141–153 (2020).
16. Fame, R. M., Cortes-Campos, C. & Sive, H. L. Brain ventricular system and cerebrospinal fluid development and function: light at the end of the tube: a primer with latest insights. *Bioessays* **42**, e1900186 (2020). 2020.
17. O'Driscoll, M. C. et al. Recessive mutations in the gene encoding the tight junction protein occludin cause band-like calcification with simplified gyration and polymicrogyria. *Am. J. Hum. Genet.* **87**, 354–364 (2010).
18. Al-Dosari, M. S. et al. Mutation in MPDZ causes severe congenital hydrocephalus. *J. Med. Genet.* **50**, 54–58 (2013).
19. Sterling, N. et al. De novo variants in MPP5 cause global developmental delay and behavioral changes. *Hum. Mol. Genet.* **29**, 3388–3401 (2020).
20. Zanotta N., et al. A case of a childhood onset developmental encephalopathy with a novel de novo truncating variant in the Membrane Protein Palmitoylated 5 (MPP5) gene. *Seizure.* https://doi.org/10.1016/j.seizure.2023.01.015 (2023).

21. Bendriem R. M., Singh S., Aleem A. A., Antonetti D. A., Ross M. E. Tight junction protein occludin regulates progenitor self-renewal and survival in developing cortex. *Elife*. **8**. https://doi.org/10.7554/eLife.49376 (2019).

22. Abdel-Hamid, M. S., Abdel-Salam, G. M. H., Issa, M. Y., Emam, B. A. & Zaki, M. S. Band-like calcification with simplified gyration and polymicrogyria: report of 10 new families and identification of five novel OCLN mutations. *J. Hum. Genet*. **62**, 553–559 (2017).

23. Kim, S. et al. The apical complex couples cell fate and cell survival to cerebral cortical development. *Neuron* **66**, 69–84 (2010).

24. Yamaguchi, M., Imai, F., Tonou-Fujimori, N. & Masai, I. Mutations in N-cadherin and a Stardust homolog, Nagie oko, affect cell-cycle exit in zebrafish retina. *Mech. Dev*. **127**, 247–264 (2010).

25. Assemat, E., Bazellieres, E., Pallesi-Pocachard, E., Le Bivic, A. & Massey-Harroche, D. Polarity complex proteins. *Biochim. Biophys. Acta* **1778**, 614–630 (2008).

26. Tepass, U., Theres, C. & Knust, E. crumbs encodes an EGF-like protein expressed on apical membranes of Drosophila epithelial cells and required for organization of epithelia. *Cell* **61**, 787–799 (1990).

27. Adachi, M. et al. Similar and distinct properties of MUPP1 and Patj, two homologous PDZ domain-containing tight-junction proteins. *Mol. Cell Biol*. **29**, 2372–2389 (2009).

28. Saugier-Veber, P. et al. Hydrocephalus due to multiple ependymal malformations is caused by mutations in the MPDZ gene. *Acta Neuropathol. Commun*. **5**, 36 (2017).

29. Feldner, A. et al. Loss of Mpdz impairs ependymal cell integrity leading to perinatal-onset hydrocephalus in mice. *EMBO Mol. Med*. **9**, 890–905 (2017).

30. Yang J., et al. Murine MPDZ-linked hydrocephalus is caused by hyperpermeability of the choroid plexus. *EMBO Mol. Med*.**11** https://doi.org/10.15252/emmm.201809540 (2019).

31. Serra, R. & Simard, J. M. Adherens, tight, and gap junctions in ependymal cells: a systematic review of their contribution to CSF-brain barrier. *Front. Neurol*. **14**, 1092205 (2023).

32. Shah, P. T. et al. Single-cell transcriptomics and fate mapping of ependymal cells reveals an absence of neural stem cell function. *Cell* **173**, 1045–1057.e9 (2018).

33. Eze, U. C., Bhaduri, A., Haeussler, M., Nowakowski, T. J. & Kriegstein, A. R. Single-cell atlas of early human brain development highlights heterogeneity of human neuroepithelial cells and early radial glia. *Nat. Neurosci*. **24**, 584–594 (2021).

34. Boroviak, T. & Rashbass, P. The apical polarity determinant Crumbs 2 is a novel regulator of ESC-derived neural progenitors. *Stem Cells* **29**, 193–205 (2011).

35. Jumper, J. et al. Highly accurate protein structure prediction with AlphaFold. *Nature* **596**, 583–589 (2021).

36. Varadi, M. et al. AlphaFold Protein Structure Database: massively expanding the structural coverage of protein-sequence space with high-accuracy models. *Nucleic Acids Res*. **50**, D439–D444 (2022).

37. Wu, X. et al. Insights regarding guanine nucleotide exchange from the structure of a DENN-domain protein complexed with its Rab GTPase substrate. *Proc. Natl Acad. Sci. USA* **108**, 18672–18677 (2011).

38. Liu, X., Bolteus, A. J., Balkin, D. M., Henschel, O. & Bordey, A. GFAP-expressing cells in the postnatal subventricular zone display a unique glial phenotype intermediate between radial glia and astrocytes. *Glia* **54**, 394–410 (2006).

39. Garcia, A. D., Doan, N. B., Imura, T., Bush, T. G. & Sofroniew, M. V. GFAP-expressing progenitors are the principal source of constitutive neurogenesis in adult mouse forebrain. *Nat. Neurosci*. **7**, 1233–1241 (2004).

40. Zhang, X. Z. et al. Folic acid rescues valproic acid-induced morphogenesis inhibition in neural rosettes derived from human pluripotent stem cells. *Front. Cell Neurosci*. **16**, 888152 (2022).

41. Fedorova, V. et al. Differentiation of neural rosettes from human pluripotent stem cells in vitro is sequentially regulated on a molecular level and accomplished by the mechanism reminiscent of secondary neurulation. *Stem Cell Res*. **40**, 101563 (2019).

42. Townshend, R. F. et al. Effect of cell spreading on rosette formation by human pluripotent stem cell-derived neural progenitor cells. *Front. Cell Dev. Biol*. **8**, 588941 (2020).

43. Grill, S. W. & Hyman, A. A. Spindle positioning by cortical pulling forces. *Dev. Cell* **8**, 461–465 (2005).

44. Guemez-Gamboa, A. et al. Loss of protocadherin-12 leads to diencephalic-mesencephalic junction dysplasia syndrome. *Ann. Neurol*. **84**, 638–647 (2018).

45. Accogli, A. et al. PCDH12 variants are associated with basal ganglia anomalies and exudative vitreoretinopathy. *Eur. J. Med. Genet*. **65**, 104405 (2022).

46. Fazeli, W. et al. The phenotypic spectrum of PCDH12 associated disorders—five new cases and review of the literature. *Eur. J. Paediatr. Neurol*. **36**, 7–13 (2022).

47. Romaniello, R. et al. Tubulin genes and malformations of cortical development. *Eur. J. Med Genet* **61**, 744–754 (2018).

48. Hung K. L., Lu J. F., Su D. J., Hsu S. J., Wang L. C. Tubulinopathy presenting as developmental and epileptic encephalopathy. *Children* **9**. https://doi.org/10.3390/children9081105 (2022).

49. Brock, S. et al. Defining the phenotypical spectrum associated with variants in TUBB2A. *J. Med. Genet*. **58**, 33–40 (2021).

50. Lee, Y. H. & Park, N. H. A complex cortical malformation caused by a mutation in the tubulin-encoding TUBB3 gene. *Taehan Yongsang Uihakhoe Chi* **81**, 1246–1249 (2020).

51. Maillard, C. et al. Tubulin mutations in human neurodevelopmental disorders. *Semin Cell Dev. Biol*. **137**, 87–95 (2023).

52. Saillour, Y. et al. LIS1-related isolated lissencephaly: spectrum of mutations and relationships with malformation severity. *Arch. Neurol*. **66**, 1007–1015 (2009).

53. Teissier, N. et al. Cytomegalovirus-induced brain malformations in fetuses. *J. Neuropathol. Exp. Neurol*. **73**, 143–158 (2014).

54. Vivarelli, R. et al. Pseudo-TORCH syndrome or Baraitser-Reardon syndrome: diagnostic criteria. *Brain Dev*. **23**, 18–23 (2001).

55. Tessier, A. et al. Bi-allelic variations in CRB2, encoding the crumbs cell polarity complex component 2, lead to non-communicating hydrocephalus due to atresia of the aqueduct of sylvius and central canal of the medulla. *Acta Neuropathol. Commun*. **11**, 29 (2023).

56. Lamont, R. E. et al. Expansion of phenotype and genotypic data in CRB2-related syndrome. *Eur. J. Hum. Genet*. **24**, 1436–1444 (2016).

57. Slavotinek, A. et al. CRB2 mutations produce a phenotype resembling congenital nephrosis, Finnish type, with cerebral ventriculomegaly and raised alpha-fetoprotein. *Am. J. Hum. Genet*. **96**, 162–169 (2015).

58. Gloerich, M., Bianchini, J. M., Siemers, K. A., Cohen, D. J. & Nelson, W. J. Cell division orientation is coupled to cell-cell adhesion by the E-cadherin/LGN complex. *Nat. Commun*. **8**, 13996 (2017).

59. Peyre, E. et al. A lateral belt of cortical LGN and NuMA guides mitotic spindle movements and planar division in neuroepithelial cells. *J. Cell Biol*. **193**, 141–154 (2011).

60. Zheng, Z. et al. LGN regulates mitotic spindle orientation during epithelial morphogenesis. *J. Cell Biol*. **189**, 275–288 (2010).

61. Konno, D. et al. Neuroepithelial progenitors undergo LGN-dependent planar divisions to maintain self-renewability during mammalian neurogenesis. *Nat. Cell Biol*. **10**, 93–101 (2008).

62. Du, Q., Taylor, L., Compton, D. A. & Macara, I. G. LGN blocks the ability of NuMA to bind and stabilize microtubules. A mechanism for mitotic spindle assembly regulation. *Curr. Biol*. **12**, 1928–1933 (2002).

63. Woodruff, J. B., Drubin, D. G. & Barnes, G. Dynein-driven mitotic spindle positioning restricted to anaphase by She1p inhibition of dynactin recruitment. *Mol. Biol. Cell* **20**, 3003–3011 (2009).

64. Mora-Bermudez, F., Matsuzaki, F. & Huttner, W. B. Specific polar subpopulations of astral microtubules control spindle orientation and symmetric neural stem cell division. *Elife* **3**, e02875 (2014).

65. Taverna, E. et al. Non-canonical features of the Golgi apparatus in bipolar epithelial neural stem cells. *Sci. Rep.* **6**, 21206 (2016).

66. Taverna, E. & Huttner, W. B. The Golgi apparatus in polarized neuroepithelial stem cells and their progeny: canonical and non-canonical features. *Results Probl. Cell Differ.* **67**, 359–375 (2019).

67. Jean, F., Stuart, A. & Tarailo-Graovac, M. Dissecting the genetic and etiological causes of primary microcephaly. *Front. Neurol.* **11**, 570830 (2020).

68. Knoblich, J. A. Mechanisms of asymmetric stem cell division. *Cell* **132**, 583–597 (2008).

69. Aaku-Saraste, E., Oback, B., Hellwig, A. & Huttner, W. B. Neuroepithelial cells downregulate their plasma membrane polarity prior to neural tube closure and neurogenesis. *Mech. Dev.* **69**, 71–81 (1997).

70. Aaku-Saraste, E., Hellwig, A. & Huttner, W. B. Loss of occludin and functional tight junctions, but not ZO-1, during neural tube closure–remodeling of the neuroepithelium prior to neurogenesis. *Dev. Biol.* **180**, 664–679 (1996).

71. Sobreira, N., Schiettecatte, F., Valle, D. & Hamosh, A. GeneMatcher: a matching tool for connecting investigators with an interest in the same gene. *Hum. Mutat.* **36**, 928–930 (2015).

72. Landrum, M. J. et al. ClinVar: improving access to variant interpretations and supporting evidence. *Nucleic Acids Res.* **46**, D1062–D1067 (2018).

73. McLaren, W. et al. Deriving the consequences of genomic variants with the Ensembl API and SNP effect predictor. *Bioinformatics* **26**, 2069–2070 (2010).

74. Chirita-Emandi, A., Doros, G., Simina, I. J., Gafencu, M. & Puiu, M. Head circumference references for school age children in western Romania. *Rev. Med. Chir. Soc. Med Nat. Iasi* **119**, 1083–1091 (2015).

75. Chen C. X. et al. A multistep workflow to evaluate newly generated ipscs and their ability to generate different cell types. *Methods Protoc.* **4**. https://doi.org/10.3390/mps4030050 (2021).

76. Okita, K. et al. A more efficient method to generate integration-free human iPS cells. *Nat. Methods* **8**, 409–412 (2011).

77. Hauser, S. et al. Establishment of SPAST mutant induced pluripotent stem cells (iPSCs) from a hereditary spastic paraplegia (HSP) patient. *Stem Cell Res.* **17**, 485–488 (2016).

78. Johannessen, C. M. et al. COT drives resistance to RAF inhibition through MAP kinase pathway reactivation. *Nature* **468**, 968–972 (2010).

79. Chilov, D. et al. Phosphorylated beta-catenin localizes to centrosomes of neuronal progenitors and is required for cell polarity and neurogenesis in developing midbrain. *Dev. Biol.* **357**, 259–268 (2011).

80. LaFave, M. C., Varshney, G. K., Vemulapalli, M., Mullikin, J. C. & Burgess, S. M. A defined zebrafish line for high-throughput genetics and genomics: NHGRI-1. *Genetics* **198**, 167–170 (2014).

81. Varshney, G. K. et al. A high-throughput functional genomics workflow based on CRISPR/Cas9-mediated targeted mutagenesis in zebrafish. *Nat. Protoc.* **11**, 2357–2375 (2016).

82. Lin, S. J. et al. Biallelic variants in KARS1 are associated with neurodevelopmental disorders and hearing loss recapitulated by the knockout zebrafish. *Genet Med.* **23**, 1933–1943 (2021).

83. Lin, S. J. et al. Biallelic variants in WARS1 cause a highly variable neurodevelopmental syndrome and implicate a critical exon for normal auditory function. *Hum. Mutat.* **43**, 1472–1489 (2022).

84. Thisse, B. & Thisse, C. In situ hybridization on whole-mount zebrafish embryos and young larvae. *Methods Mol. Biol.* **1211**, 53–67 (2014).

85. Yushkevich, P. A. et al. User-guided 3D active contour segmentation of anatomical structures: significantly improved efficiency and reliability. *Neuroimage* **31**, 1116–1128 (2006).

86. Perez-Riverol, Y. et al. The PRIDE database resources in 2022: a hub for mass spectrometry-based proteomics evidences. *Nucleic Acids Res.* **50**, D543–D552 (2022).

Author contributions

E Banks designed, performed, and analyzed most experiments and wrote the manuscript. V Francis performed mouse immunohistochemistry, coordinated induced seizure experiments and mouse MRIs, and maintained the mouse colony. SJL performed and analyzed zebrafish experiments in Fig. 4 and Supplementary Fig. 3. F.K. established the mouse colony, performed the western blot in Fig. 3a, and coordinated mouse MRIs. V. Fonov processed and analyzed mouse MRIs. M.L. performed the induced seizure experiments. C.H. established the iPSC lines. G.K. performed RT-qPCR on mouse brain tissue for Fig. 3b. M.T. performed the mouse MRIs. A.B. analyzed mouse MRIs and provided experimental input. F.S.A. generated and provided lymphoblast cell lines and contributed to two clinical cases. S. Hauser and S.K. established iPSC lines from participants 2 and 10. R.A.K., F.S.A., L.A., M. Babaei, M. Bahlo, B.B., E. Barr, L.B., M. Bassiony, M. Bertrand, D.B., R.B., M. Budetta, M.C.D., D.G.C., H.C., D.C., S.E., M.A.E., H.G.E.S., T.F., H.K.G., J.G.G., L.G., E.S.Y.G., V.K.G., T.B.H., M.O.H., T.L.H., J.S.H., A.H., H.H., K.H., S. Huynh, E.G.K., G.C.K., A.K., H.L., J.R.L., E.J.M., A.M., D.M., J.N.F., H.N., D.M.N., B.O.J., M.O., D.P., L.G.S., C.S., L.S., V.S., R.C.S., V.M.S., P.N.T., T.T., M.S.Z., D.Z., and C.Z. completed phenotypic questionnaires and contributed to clinical phenotyping genetic analysis. K.M. acted as a liaison to connect E. Banks with clinicians who submitted variants on ClinVar. R.P. analyzed clinical exomes of GeneDx-tested cases. B.A.M. identified the initial cases. U.D.N. is associated with the contribution of data from Participant 9. K.H. and C.P. provided technical aid to F_0 zebrafish experiments. J.F.T. identified the intramolecular interface in Fig. 4 and supervised all structural analyses. T.M.D. supervised iPSC quality control and cell line production. Z.G. supervised genetic analysis. M.A. supervised induced seizure experiments. C.A. analyzed participant MRIs

and CTs. G.K.V. supervised zebrafish experiments. R.M. contributed many clinical cases and connected us with C.A., G.K.V., S.J.L., K.H., and C.P. D.A.R. supervised mouse MRI data collection and analysis. All authors reviewed the manuscript for accuracy and edited wording or data presentation according to their clinical, molecular, structural, genetic, or biological expertise. P.S.M. supervised the study, designed experiments, secured funding, and wrote the manuscript.

Competing interests

K.M. and R.P. are employed by GeneDx, LLC. All other authors report no competing interests.

Additional information

Emily Banks [1], Vincent Francis[1], Sheng-Jia Lin [2], Fares Kharfallah[1], Vladimir Fonov [1], Maxime Lévesque [1], Chanshuai Han[1], Gopinath Kulasekaran[1], Marius Tuznik[1], Armin Bayati [1], Reem Al-Khater [3], Fowzan S. Alkuraya [4], Loukas Argyriou[5], Meisam Babaei[6], Melanie Bahlo [7], Behnoosh Bakhshoodeh[8], Eileen Barr [9], Lauren Bartik[10,11], Mahmoud Bassiony [12], Miriam Bertrand[13], Dominique Braun [14], Rebecca Buchert [13], Mauro Budetta[15], Maxime Cadieux-Dion[16], Daniel G. Calame[17,18,19], Heidi Cope[20], Donna Cushing[21], Stephanie Efthymiou [22], Marwa Abd Elmaksoud [23], Huda G. El Said[23], Tawfiq Froukh [24], Harinder K. Gill[25], Joseph G. Gleeson [26,27], Laura Gogoll[14], Elaine S.-Y. Goh [21], Vykuntaraju K. Gowda [28], Tobias B. Haack [13], Mais O. Hashem[4], Stefan Hauser [29,30], Trevor L. Hoffman[31], Jacob S. Hogue[32], Akimoto Hosokawa[33], Henry Houlden [22], Kevin Huang [2], Stephanie Huynh[25], Ehsan G. Karimiani[34,35], Silke Kaulfuß[5], G. Christoph Korenke[36], Amy Kritzer[37], Hane Lee [38], James R. Lupski [17,18,19,39], Elysa J. Marco[40], Kirsty McWalter [41], Arakel Minassian[42], Berge A. Minassian[43], David Murphy[44], Juanita Neira-Fresneda[9], Hope Northrup [45], Denis M. Nyaga [33], Barbara Oehl-Jaschkowitz[46], Matthew Osmond[47], Richard Person[41], Davut Pehlivan[17,18,19], Cassidy Petree[2], Lynette G. Sadleir[33], Carol Saunders [10,16,48], Ludger Schoels[29,30], Vandana Shashi[20], Rebecca C. Spillmann[20], Varunvenkat M. Srinivasan[28], Paria N. Torbati[35], Tulay Tos[49], Undiagnosed Diseases Network*, Maha S. Zaki [50], Dihong Zhou[10,11], Christiane Zweier [14], Jean-François Trempe [51], Thomas M. Durcan[1], Ziv Gan-Or [1,52], Massimo Avoli[1], Cesar Alves[53], Gaurav K. Varshney [2], Reza Maroofian [22], David A. Rudko[1,54,55] & Peter S. McPherson [1] ✉

[1]Department of Neurology and Neurosurgery, the Neuro, McGill University, Montréal, QC, Canada. [2]Genes & Human Disease Research Program, Oklahoma Medical Research Foundation, Oklahoma City, OK, USA. [3]Johns Hopkins Aramco Healthcare, Dhahran, Saudi Arabia. [4]Department of Translational Genomics, Center for Genomic Medicine, King Faisal Specialist Hospital and Research Center, Riyadh, Saudi Arabia. [5]Institute of Human Genetics, University Medical Center, Göttingen, Germany. [6]Department of Pediatrics, North Khorasan University of Medical Sciences, Bojnurd, Iran. [7]Walter and Eliza Hall Institute for Medical Research, Parkville, VIC, Australia. [8]Mashhad University of Medical Sciences, Mashhad, Iran. [9]Department of Human Genetics, Emory University, Atlanta, GA, USA. [10]University of Missouri-Kansas City, School of Medicine, Kansas City, MO, USA. [11]Department of Pediatrics, Division of Clinical Genetics, Children's Mercy Hospital, Kansas City, MO, USA. [12]Faculty of Medicine, Alexandria University, Alexandria, Egypt. [13]Institute of Medical Genetics and Applied Genomics, University of Tübingen, Tübingen, Germany. [14]Department of Human Genetics, Inselspital, Bern University Hospital, University of Bern, Bern, Switzerland. [15]Paediatric and Child Neurology Unit, Cava de' Tirreni AOU S. Giovanni di Dio e Ruggiero d'Aragona Hospital, Salerno, Italy. [16]Department of Pathology and Laboratory Medicine, Children's Mercy Hospital, Kansas City, MO, USA. [17]Department of Pediatrics, Baylor College of Medicine, Houston, TX, USA. [18]Texas Children's Hospital, Houston, TX, USA. [19]Department of Molecular and Human Genetics, Baylor College of Medicine, Houston, TX, USA. [20]Division of Medical Genetics, Department of Pediatrics, Duke University Medical Center, Durham, NC, USA. [21]Laboratory Medicine and Genetics, Trillium Health Partners, Mississauga, ON, Canada. [22]Department of Neuromuscular Diseases, University College London (UCL) Queen Square Institute of Neurology, London, UK. [23]Neurology Unit, Department of Pediatrics, Faculty of Medicine, University of Alexandria, Alexandria, Egypt. [24]Department of Biotechnology and Genetic Engineering, Philadelphia University, Amman, Jordan. [25]Provincial Medical Genetics Program at BC Women's Health Centre, Vancouver, BC, Canada. [26]Department of Neurosciences, University of California San Diego, La Jolla, CA, USA. [27]Rady Children's Institute for Genomic Medicine, San Diego, CA, USA. [28]Department of Pediatric Neurology, Indira Gandhi Institute of Child Health, Bangalore, India. [29]German Center of Neurodegenerative Diseases (DZNE),

Tübingen, Germany. [30]Center for Neurology and Hertie Institute for Clinical Brain Research, University Tübingen, Tübingen 72076, Germany. [31]Department of Regional Genetics, Southern California Kaiser Permanente Medical Group, Anaheim, CA, USA. [32]Madigan Army Medical Center, Tacoma, WA, USA. [33]Department of Paediatrics and Child Health, University of Otago, Wellington, New Zealand. [34]Molecular and Clinical Sciences Institute, St. George's, University of London, Cranmer Terrace, London, UK. [35]Department of Medical Genetics, Next Generation Genetic Polyclinic, Mashhad, Iran. [36]Department of Neuropediatrics, University Children's Hospital, Klinikum Oldenburg, Oldenburg, Germany. [37]Division of Genetics and Genomics, Boston Children's Hospital, Boston, MA, USA. [38]3billion Inc, Seoul, South Korea. [39]Human Genome Sequencing Center, Baylor College of Medicine, Houston, TX, USA. [40]Cortica Healthcare, San Rafael, CA, USA. [41]GeneDx, Gaithersburg, MD, USA. [42]Centre for Applied Genomics, Genetics, and Genome Biology, Hospital for Sick Children, Toronto, ON, Canada. [43]Department of Pediatrics and Neurology, UT Southwestern Medical Center, Dallas, TX, USA. [44]Department of Clinical and Movement Neurosciences, University College London (UCL) Queen Square Institute of Neurology, London, UK. [45]Department of Pediatrics, McGovern Medical School at the University of Texas Health Science Center at Houston (UTHealth) and Children's Memorial Hermann Hospital, Houston, TX, USA. [46]BIOSCIENTIA-MVZ-Labor-Saar-Practice of Human Genetics, Homburg (Saar), Germany. [47]Children's Hospital of Eastern Ontario Research Institute, University of Ottawa, Ottawa, Canada. [48]Center for Pediatric Genomic Medicine Children's Mercy, Kansas City, MO, USA. [49]Department of Medical Genetics, University of Health Sciences, Zubeyde Hanim Research and Training Hospital of Women's Health and Diseases, Ankara, Turkey. [50]Human Genetics and Genome Research Institute, Clinical Genetics Department, National Research Centre, Cairo, Egypt. [51]Department of Pharmacology & Therapeutics and Centre de Recherche en Biologie Structurale, McGill University, Montréal, QC, Canada. [52]Department of Human Genetics, McGill University, Montréal, QC, Canada. [53]Division of Neuroradiology, Boston Children's Hospital, Harvard Medical School, Boston, MA, USA. [54]McConnell Brain Imaging Centre, the Neuro, Montréal, QC, Canada. [55]Department of Biomedical Engineering, McGill University, Montréal, QC, Canada. ✉e-mail: peter.mcpherson@mcgill.ca

Undiagnosed Diseases Network

Heidi Cope[20]

A full list of members and their affiliations appears in the Supplementary Information.